



# Influence of extrusion rate and magma rheology on the growth of lava domes: Insights from particle-dynamics modeling



Taha Husain <sup>a,b,\*</sup>, Derek Elsworth <sup>a,b</sup>, Barry Voight <sup>c</sup>, Glen Mattioli <sup>d</sup>, Pamela Jansma <sup>d</sup>

<sup>a</sup> Energy and Mineral Engineering, G3 Center, The Pennsylvania State University, University Park, PA 16802, United States

<sup>b</sup> EMS Energy Institute, The Pennsylvania State University, University Park, PA 16802, United States

<sup>c</sup> Geosciences, The Pennsylvania State University, University Park, PA 16802, United States

<sup>d</sup> Department of Earth and Environmental Sciences, University of Texas at Arlington, Arlington, TX 76019, United States

## ARTICLE INFO

### Article history:

Received 11 April 2014

Accepted 12 August 2014

Available online 20 August 2014

### Keywords:

Magma rheology

Lava dome

Emplacement dynamics

Discrete element modeling

## ABSTRACT

Lava domes are structures that grow by the extrusion of viscous silicic or intermediate composition magma from a central volcanic conduit. Repeated cycles of growth are punctuated by collapse, as the structure becomes oversized for the strength of the composite magma that rheologically stiffens and strengthens at its surface. Here we explore lava dome growth and failure mechanics using a two-dimensional particle-dynamics model. The model follows the evolution of fractured lava, with solidification driven by degassing induced crystallization of magma. The particle-dynamics model emulates the natural development of dome growth and rearrangement of the lava dome which is difficult in mesh-based analyses due to mesh entanglement effects. The deformable talus evolves naturally as a frictional carapace that caps a ductile magma core. Extrusion rate and magma rheology together with crystallization temperature and volatile content govern the distribution of strength in the composite structure. This new model is calibrated against existing observational models of lava dome growth. Results show that the shape and extent of the ductile core and the overall structure of the lava dome are strongly controlled by the infusion rate. The effects of extrusion rate on magma rheology are sensitive to material stiffness, which in turn is a function of volatile content and crystallinity. Material stiffness and material strength are key model parameters which govern magma rheology and subsequently the morphological character of the lava dome and in turn stability. Degassing induced crystallization causes material stiffening and enhances material strength reflected in non-Newtonian magma behavior. The increase in stiffness and strength of the injected magma causes a transition in the style of dome growth, from endogenous expansion of a ductile core, to stiffer and stronger intruding material capable of punching through the overlying material and resulting in the development of a spine or possibly inducing dome collapse. Simulation results mimic development of a megaspine upon the influx of fresh magma which leads to the re-direction of magma flow, creating a new shear zone and the switching of dome growth from one side to the other. Our model shows similar dome growth dynamics as observed at Soufriere Hills Volcano, Montserrat, indicating a strong correlation between extrusion rate and its subsequent effect on mechanical properties and variations in magma rheology.

© 2014 Elsevier B.V. All rights reserved.

## 1. Introduction

Silicic and intermediate composition volcanoes commonly generate lava domes, which are structures that grow by the extrusion of viscous magma from a central volcanic conduit. The solidification and rheological stiffening of magma are controlled by varying degrees of cooling and degassing-induced crystallization. Degassing-induced crystallization is a dominant process for andesitic magma systems such as at Soufrière Hills Volcano (SHV), Montserrat (Sparks, 1997; Melnik and Sparks, 1999) and Merapi Volcano, Indonesia (Hammer et al., 2000; Innocenti et al., 2013a,b). Degassing results in rheological stiffening of magma, which in turn is a consequence of gas exsolution that triggers

crystallization of microlites from undercooled melt (Hort, 1998; Melnik and Sparks, 1999; Cashman and Blundy, 2000; Hammer and Rutherford, 2002; Melnik and Sparks, 2002; Woods and Huppert, 2003). The volume fraction of melt and crystal content in the magma control its bulk viscosity (Hess and Dingwell, 1996; Costa, 2005; Melnik and Sparks, 2005). This volume fraction changes with pressure and magma flow rate, and the resulting morphology of a lava dome can be affected (Watts et al., 2002; Melnik et al., 2005).

Of fundamental importance to understanding many volcanic processes as well as mitigating volcanic hazard is detailed knowledge of the conditions required for dome collapse (Voight and Elsworth, 1997, 2000). Causal mechanisms and triggers contributing to individual collapse events include oversteepening of slopes, rainfall-driven gravitational collapse (Elsworth and Voight, 1992; Barclay et al., 1998; Carn

\* Corresponding author at: 230 A Hosler, University Park, PA - 16802, United States.

**Table 1**  
Notation.

Symbol	Description	Unit
$Q_{3D}$	Flow rate in 3D geometry	$L^3 T^{-1}$
$v_{3D}$	Flow velocity of fluid for 3D geometry	$L T^{-1}$
$a_{3D}$	Area of conduit for a 3D geometry	$L^2$
$v_{3D}^{avg}$	Average fluid velocity given by Hagen–Poiseuille's flow equation	$L T^{-1}$
$r$	Radius of conduit	$L$
$f_n$	Normal force applied on the particle in contact with another in PFC2D	$M L T^{-2}$
$k_n$	Normal contact bond stiffness	$M T^{-2}$
$\delta_n$	Overlap in the normal direction between 2 contacting particle in PFC2D	$L$
$f_s$	Shear force applied on the contacting particle in PFC2D	$M L T^{-2}$
$k_s$	Shear contact bond stiffness	$M T^{-2}$
$\delta_s$	Particle overlap in the shear direction in PFC2D	$L$
$C$	Material cohesion	$M L^{-1} T^{-2}$
$\mu$	Coefficient of friction of the material	–
$\sigma_{max}$	Tensile strength of the material	$M L^{-1} T^{-2}$
$\Delta L$	Change in length on application of normal force on the sample/particle	$L$
$L_0$	Original length of the sample/particle	$L$
$D$	Original diameter of the sample/particle	$L$
$E$	Young's modulus	–
$E_c$	Microscopic modulus for particle–particle contact bond	–
$E_p$	Microscopic modulus for parallel bond	–
$\zeta_c$	Ratio of microscopic modulus to macroscopic modulus for particle–particle contact bond	–
$\zeta_p$	Ratio of microscopic modulus to macroscopic modulus for parallel bond	–
$G$	Shear modulus	–
$\Delta x$	Change in length of the sample/particle in the shear direction	$L$
$\eta$	Fluid viscosity	$M L^{-1} T^{-1}$
$k^n, k^s$	Parallel bond normal and shear stiffness respectively	$M L^{-2} T^{-2}$
$\Delta U^s$	Shear displacement for a given time step $\Delta t$	$L$
$V_i$	Shear velocity for the given time step $\Delta t$	$L T^{-1}$
$y$	Length of sample/particle in the direction perpendicular to shear displacement	$L$
$w_c$	Characteristic width of the conduit to represent the 3D flow rate to its representative value for the 2D geometry	$L$
$\phi$	Friction angle of the material	–
$A$	Area on which force is applied	$L^2$
$A_0$	Area of sample/particle before deformation	$L^2$
$\tau_{max}$	Shear strength of the material	$M L^{-1} T^{-2}$
$ V $	Numerical value of pure shear force applied	$M L T^{-2}$
$T_{liq,sol}$	Temperature of the magma in the solution state	–
$T_{solidus}$	Temperature of the magma below which the magma solidifies for a given pressure	–
$p$	External pressure acting on the magma during the eruption cycle	$M L^{-1} T^{-2}$
$a_T$	Constant for the empirical expression to obtain the phase behavior of the magma at Soufrière Hills Volcano, Montserrat	–
$b_T$	Constant for the empirical expression to obtain the phase behavior of the magma at Soufrière Hills Volcano, Montserrat	–
$c_T$	Constant for the empirical expression to obtain the phase behavior of the magma at Soufrière Hills Volcano, Montserrat	–
$d_T$	Constant for the empirical expression to obtain the phase behavior of the magma at Soufrière Hills Volcano, Montserrat	–

et al., 2004; Elsworth et al., 2004; Simmons et al., 2004) and internal forcing and gas pressurization (Elsworth and Voight, 1995; Voight and Elsworth, 2000; Elsworth and Voight, 2001; Simmons et al., 2005). For a more comprehensive listing of mechanisms see Voight and Elsworth (1997) (Table 1).

One of the most basic influences on dome stability, the interior structure of a dome, is in general poorly understood (e.g. Hale and Wadge, 2003). The exact mechanical response of the volcanic edifice to magma intrusion is not clear (Annen et al., 2001) despite numerous studies to predict growth and eruption state (Anderson and Fink, 1990; Blake, 1990; Fink and Griffiths, 1990; Fink et al., 1990; Iverson, 1990; Swanson and Holcomb, 1990; Griffiths and Fink, 1993; Elsworth and Voight, 1995; Griffiths and Fink, 1997; Buisson and Merle, 2004; Elsworth et al., 2004). Quantifying the extent to which parameters such as extrusion and cooling rates and material properties including coefficient of friction, cohesive strength and dynamically evolving magma viscosity that control the morphology is important (Blake, 1990; Griffiths and Fink, 1997; Shen, 1998). Because the collapse of lava domes can produce devastating and deadly pyroclastic flows, a quantitative model of the internal structure of the lava dome is desired.

The focus of many previous studies was to predict the flow pattern and most importantly the eruption state of the evolving lava dome (e.g. Anderson and Fink, 1990; Griffiths and Fink, 1997; Shen, 1998). Available data aid the development of more sophisticated models that incorporate an improved understanding of the physics and rheology of the repeated growth and destruction of lava domes (Huppert et al.,

1982; Fink and Griffiths, 1990; Iverson, 1990; Griffiths and Fink, 1993; Griffiths, 2000; Buisson and Merle, 2002; Buisson and Merle, 2004; Melnik et al., 2005; Morgan and McGovern, 2005a; Simmons et al., 2005; Hale and Mühlhaus, 2007; Hale et al., 2007; Hale and Wadge, 2008). Some of the previous models illuminate mechanisms that cause a transition from endogenous to exogenous lava dome growth. This transition of lava dome growth from endogenous to exogenous may be critical as it often coincides with significant changes in the extrusion rate and is a prelude to hazardous lava dome collapse events (Watts et al., 2002).

Here we use a two-dimensional numerical model to investigate dome growth on a horizontal surface where growth occurs about the axis of the conduit. The 2D model only considers two force components (neglecting the out-of-plane component for the calculations using the equation of motion and the force–displacement laws) and a moment component, unlike the case of a 3D model (3 components each of force and moment). This model uses the discrete element method (DEM) (Cundall and Strack, 1979) to represent the injection of magma into a central fluid core that evolves on its margins into a brittle

**Table 2**  
Dimensions of the model.

Conduit length (2D)	Equivalent conduit radius (3D)	Conduit width (2D)	Depth of conduit (2D)	Expanse of the base
30 m	15 m	23.5725 m	600 m	600 m

carapace of talus. We follow the evolution of the synthetic dome, to decipher the principal mechanisms contributing to the resulting dome morphology and potential instability. This is the first investigation of lava domes using this powerful modeling approach; here we explore the simplest case, but in the future more complex 2D and 3D geometries will be examined.

**2. Model description**

We represent the lava as an aggregate of discrete particles representative of “packets of magma” using the discrete element method (Cundall and Strack, 1979). This model is developed in the code PFC<sup>2D</sup> which incorporates granular contact mechanics capable of mapping the stress distribution in a deforming aggregate. The code uses soft particle dynamics to incorporate elastic deformation localized at particle–particle contacts with the interparticle contact laws playing an important role in defining the behavior of the assemblage (Morgan and McGovern, 2005a,b).

The lava dome grows on a rigid horizontal substrate fed by flow through a vertical conduit. The magma packets are idealized as particles of arbitrary radius (1.5 m in this study). Flow velocity ( $v_{3D}^{avg}$ ) of the magma packets through the magma conduit is given as,

$$v_{3D}^{avg} = Q_{3D} / \pi r^2 \tag{1}$$

where  $Q_{3D}$  is the specified flow rate in 3D configuration and the cross-section area of the conduit of radius  $r$  is  $a_{3D} = \pi r^2$ . Dimensions of the conduit for the 2D model are given in Table 2.

The 2D model treats the particles as cylinders for stress calculations, where the centroids of all the cylinders lie in the same plane. The cross-sectional area of the conduit for the 2D and 3D model are equal. The expression for characteristic/effective width ( $w_c$ ) for the specified conduit length (equal to  $2r$ ) is discussed in the Appendix A (Fig. 1c & d). Fig. 2 represents the basic geometry of the simulation model. The flow velocity in the 2D model is specified equal to the 3D value given by Eq. (1) for a given 3D flow rate.

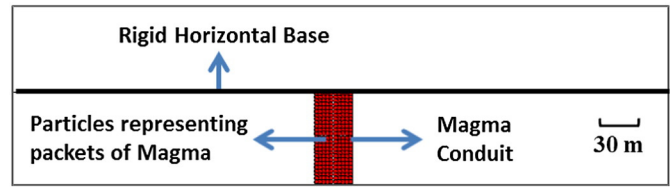


**Fig. 2.** Basic cross-sectional setup of the PFC<sup>2D</sup> model which includes the conduit (30 m length with rigid walls) where the lava dome develops on a rigid horizontal surface (300 m long on either side of the conduit) and the red particles of 1.5 m radius represent magma that forms the cohesion dominated core in the lava dome.

The constitutive law for particle–particle/wall–particle contacts in the aggregate is the linear contact model, which governs the morphology of the aggregate by correlating the material stiffness with contact stiffness. Repulsive contact force in normal ( $f_n$ ) and shear ( $f_s$ ) directions are

$$f_n = k_n \delta_n \tag{2}$$

$$f_s = k_s \delta_s \tag{3}$$

where  $k_n$  and  $k_s$  are the contact stiffnesses in the normal and shear direction, while particle overlap in the respective directions are represented by  $\delta_n$  and  $\delta_s$  in Eqs. (2) and (3). The normal ( $k_n$ ) and shear ( $k_s$ ) contact stiffness are related to the material properties as

$$k_n = E(w_c) \tag{4}$$

$$k_s = G(w_c) \tag{5}$$

where  $E$  is the Young’s modulus and  $G$  is the shear modulus of the particle assemblage in the absence of a parallel bond. The characteristic width ( $w_c$ ) in Eqs. (4) and (5) is the parameter that correlates the flow rate of the 3D geometry to its representative 2D value (see Appendix A). The particle overlap is controlled by the Young’s and

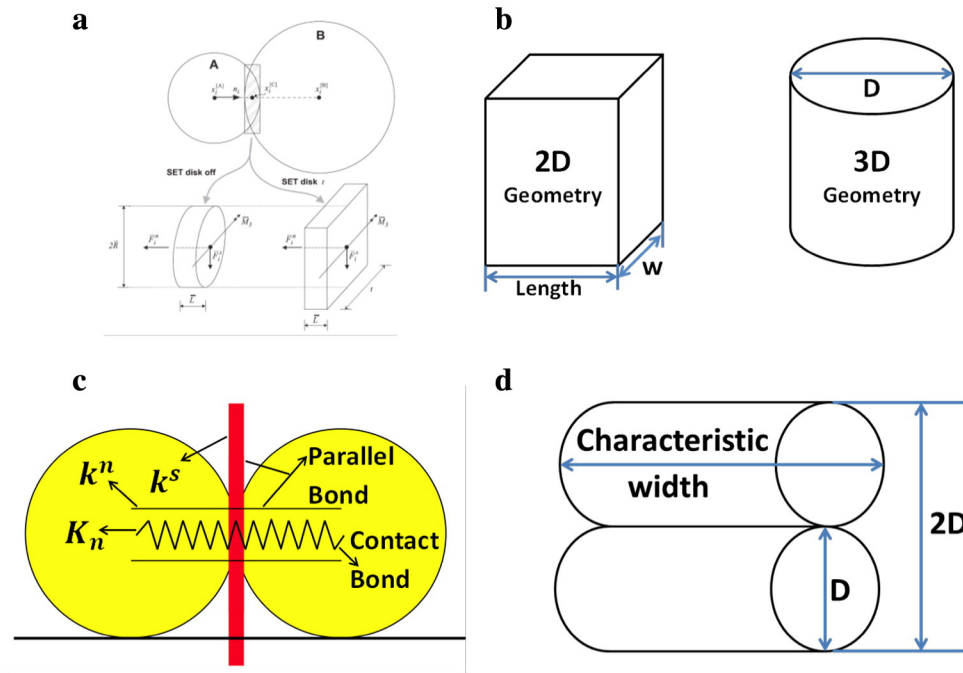


**Fig. 1.** a) Parallel bond depicted as a finite-sized piece of cementitious material (Itasca Consulting Group, 2004). b) Location of the linear contact bond and parallel bond in the PFC2D code. c) Conduit geometry in 2D correlated with the 3D geometry ( $w$  is the characteristic width of the 2D geometry which correlates the 3D flow rate to a representative value in 2D). d) Shape of the particle used in the simulation run and area perpendicular to applied force.

**Table 3**

Constant for the empirical expression obtained for the phase behavior of magma (Melnik and Sparks, 2005).

Constant	Liquidus	Solidus
$a_T$	1465.5	1252.2
$b_T$	-31.4	-25.3
$c_T$	-2.8	-11.9
$d_T$	-0.41	1.17

shear moduli of the material. The contact shear force is limited by the Mohr–Coulomb failure criterion and the maximum shear force ( $f_s^{max}$ ) is given by

$$f_s^{max} = C + \mu f_n \tag{6}$$

where  $C$  is the material cohesion, coefficient of friction is  $\mu$ , and  $f_n$  is normal contact force. Material cohesion ( $C$ ) is an important parameter and affects the simulated dome growth pattern significantly. Cohesion is represented by parallel bond strength/rigidity in the model. A parallel bond approximates the physical behavior of two bonded particles where torsion of the assemblage is resisted (as represented in Fig. 1a & b) (Delenne et al., 2004; Itasca Consulting Group, 2004; Guo and Morgan, 2006). Maximum normal ( $\sigma_{max}$ ) and shear strength ( $\tau_{max}$ ) for failure of the parallel bond is given as

$$\sigma_{max} = T/A \tag{7}$$

$$\tau_{max} = |V|/A \tag{8}$$

where the macro-response of a parallel bond is related to that of an elastic beam of area  $A$ , subject to pure axial ( $T$ ) and pure shear loading ( $|V|$ ) given by Eqs. (7) and (8). The parallel bond breaks when the pure axial or shear stress applied on the bond exceeds the bond strength.

Parallel bonds exist between adjacent particles (Fig. 1a & b) and restrict particles from rotating relative to each other – this is analogous to limiting fluid vorticity to achieve irrotational flow. Relative motion at the particle contacts result in the development of a force and moment within the modeled aggregate, conditioned by the parallel-bond stiffness. Parallel bonds transmit force as well as moment between two bonded particles. Schematically, a parallel bond is a set of elastic springs defined by normal and shear stiffnesses that support a portion of the

force applied on the modeled particle structure. Thus, the effective stiffness of the modeled aggregate depends on the parallel bond stiffness and the linear contact stiffness. The composite Young’s modulus ( $E$ ) of the aggregate in the presence of a parallel bond is given as,

$$E = E_c/\zeta_c + E_p/\zeta_p \tag{9}$$

where  $E_c$  and  $E_p$  are the Young’s moduli for the particle–particle and parallel bond contacts respectively, while  $\zeta_c$  and  $\zeta_p$  are the ratios of microscopic modulus to macroscopic modulus for the particle–particle (linear contact) and parallel bond respectively. The correlation of microscopic moduli ( $E_c$  and  $E_p$ ) is given in the Appendix A. The ratios of the moduli for a particle system are calculated by initially assigning only linear contact bonds to the particles ( $E_p = 0$ ) to obtain the value of  $\zeta_c$ . The other ratio ( $\zeta_p$ ) is obtained by repeating this procedure and only assigning parallel bonds to the particles. In the absence of a parallel bond, the value of the macroscopic Young’s modulus ( $E$ ) for the system is equal to the microscopic particle–particle linear contact modulus given in Eq. (4) (Itasca Consulting Group, 2004). Therefore, addition of the parallel bond to the particle–particle assembly increases the effective stiffness of the modeled particle aggregate (Fig. 1b). The parallel bond breaks when the applied force exceeds the maximum normal or shear stress (bond strength), as given by Eqs. (7) and (8) which results in the progressive reduction of the bulk elastic modulus. The material accumulates damage as parallel bonds are broken. An increase in the ratio of parallel bond stiffness to contact stiffness increases the rate at which damage accumulates in the material when strained (Itasca Consulting Group, 2004). The parallel bonded material with higher parallel bond shear stiffness behaves in a manner analogous to a highly viscous fluid. The correlation of viscosity with parallel bond shear stiffness is given in the Appendix A.

The dominant mode of deformation is influenced by mechanical properties of the particle assemblage. The coefficient of friction and cohesion manifest through the Coulomb yield criterion and material stiffness control deformation behavior (Morgan and McGovern, 2005a). The bulk composition of the magma is strongly influenced by temperature and comprises silicate melt, crystals and volatiles – the relative proportion of these fractions exerts a significant influence on material stiffness. Viscosity and density both change due to progressive gas exsolution from the melt and subsequent gas loss during conduit flow and extrusion. This effect may be parameterized as a function of dissolved water in the melt, crystal content and pressure (Melnik and Sparks, 2005). The model accounts for changes in magma liquidus temperature

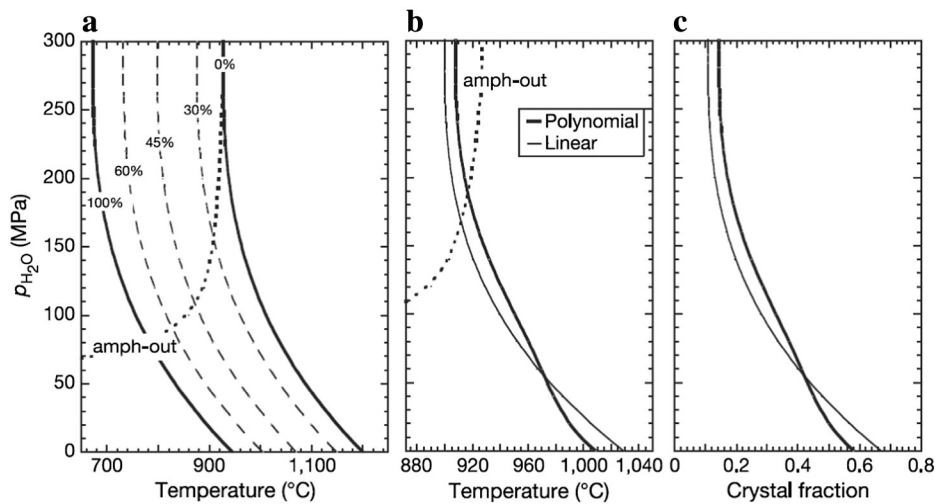


**Fig. 3.** Modeled variation in magmatic parameters during decompression of water saturated silicic andesite. Magma is similar in composition to Mount St. Helens and Mount Pinatubo. (a) Phase diagram for water saturated magma at 220 MPa with crystal fraction contours. (b) Temperature variation based on linear variation between liquidus and solidus. (c) Crystal fraction based on linear and polynomial variation for crystal free magma at 300 MPa and initial temperature of 880 °C (Blundy et al., 2006).

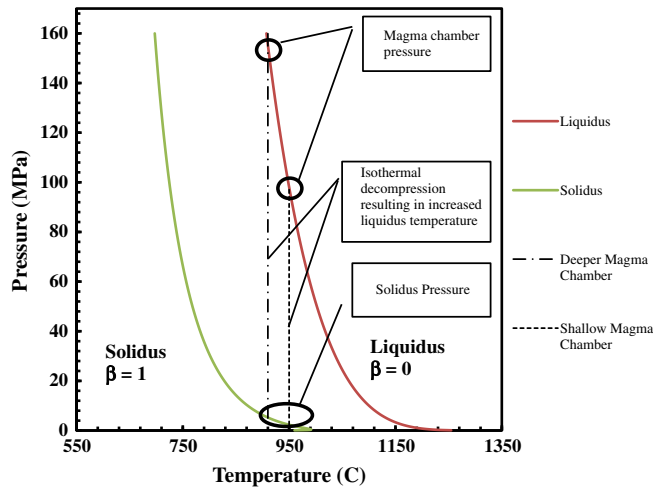


**Fig. 4.** Phase behavior of magma with variation in pressure and temperature obtained using Eq. (9) for an experimental sample at 160 MPa and 875 °C (initial pressure and temperature) with composition similar to the dome lava obtained at Soufrière Hills Volcano, Montserrat ( $\beta$  indicates crystal content in the material) (Couch et al., 2003; Melnik and Sparks, 2005).

which results from exsolution of water from the melt and changes in melt phase chemical composition during crystallization. Experiments on the crystallization of plagioclase feldspar, the major crystallizing phase during decompression of andesite magmas, provide an empirical correlation between magma liquidus/solidus temperature ( $T_{liq,sol}$ ) (Couch et al., 2003; Melnik and Sparks, 2005). This may be parameterized as

$$T_{liq,sol} = a_T + b_T \ln(p) + c_T \ln(p)^2 + d_T \ln(p)^3 \quad (10)$$

noting the dominant influence of pressure and modulated by empirical constants  $a_T$ ,  $b_T$ ,  $c_T$  and  $d_T$ . A least-squares best fit to the experimental data, defined by Eq. (10), yields the values of the constants ( $a_T$ ,  $b_T$ ,  $c_T$  and  $d_T$ ) given in Table 3. These differ for the liquid and solid states depending on the extent of crystallization. Lava solidification is related to pressure using the solidus temperature ( $T_{solidus}$ ) which is given by Eq. (10).

Fig. 3 represents the phase behavior of the ascending andesitic magma with crystal fraction increasing with a reduction in pressure which results in the decrease of the weight percentage of dissolved water in the magma (Blundy et al., 2006).

There are two mechanisms that result in the solidification of magma: (1) cooling of the extruded lava surface yielding a solid exterior crust, which in turn leads to rheological stiffening (Fink and Griffiths, 1990; Iverson, 1990); and (2) gas exsolution during magma ascent

increases the magma liquidus temperature promoting crystallization and resulting in solidification (Hort, 1998; Cashman and Blundy, 2000; Couch et al., 2003; Blundy et al., 2006). Degassing-induced crystallization is the dominant mechanism controlling the emplacement of intermediate composition (andesite or dacite) lavas (Hammer et al., 2000; Sparks et al., 2000). Crystallinity and magma liquidus temperature both increase with decreasing partial pressure of  $H_2O$  (Fig. 3a, b, c) (Blundy et al., 2006). Fig. 4 illustrates the increase in the magma liquidus and solidus temperature as magma ascends isothermally to the surface through the conduit. As decompressing magma exsolves gas, the liquidus temperature increases resulting in increased undercooling that triggers crystallization and leads to the rheological stiffening of the magma. Experiments conducted on rhyolitic melts with similar compositions to that of the ongoing eruption of the Soufrière Hills Volcano (SHV) suggest an undercooling of about 150–200 °C for a melt with dissolved water content of ~4% (Barclay et al., 1998). Exsolution of volatiles causes melt viscosity to increase by several orders of magnitude (Dingwell et al., 1996). Highly crystalline magma develops strong non-Newtonian properties and mechanical strength. Accordingly, the decompression path that the magma experiences governs the kinetics of crystallization and thus plays an important role in controlling the texture of the crystallizing magma. Matrix glass composition may be used to obtain the pressure at which glass and crystal attain equilibrium and thus to track groundmass crystallinity (Blundy and Cashman, 2001). Melt composition is used to obtain effective pressure at which crystal growth kinetics are inhibited and the melt chemistry is considered as frozen. In some studies, this pressure is termed the “closure pressure” and is controlled by the kinetics of crystal nucleation and growth (Cashman and Blundy, 2000). In general, magma rheology strongly depends on the depth and time taken by the melt to attain closure pressure (Sparks et al., 2000).

The transition of the soft core of the simulated lava dome (indicated by red particles, Fig. 2) from a liquid mush to a solid state (which breaks into fractured lava and is indicated by yellow particles) is represented through the solidus/closure pressure (Simmons et al., 2005). Eq. (10) is an empirical expression that gives liquidus and solidus pressures respectively, as depicted in Fig. 4 (Melnik and Sparks, 2005; Hale, 2008). Magma ascending to the surface experiences a reduction in pressure which results in the exsolution of volatiles. As this pressure approaches the solidus/closure pressure the liquidus temperature rises and crystallization is promoted by magma undercooling. The crystallization history of the magma is frozen at the solidus/closure pressure, where the magma is now completely solid. In our model the pressure exerted on each discrete particle is tracked and if the value is equal to or below the solidus pressure, material properties of that particle are changed to match the values of a crystallized solid of appropriate composition. The transition from core (cohesion dominated and ductile) to solidified lava (friction dominated) is a binary step-change in properties and is unidirectional — an increase in pressure will not enable a return

**Table 4**

Input parameters for model runs in Figs. 8–11 to obtain modeled lava dome morphology for limiting range of values.

Parameter	Figs. 8 and 10		Figs. 9 and 11	
	Low	High	Low	High
Flow rate ( $m^3/s$ )	0.5	0.5	10	10
Density ( $kg/m^3$ )	2500	2500	2500	2500
Solidus pressure (MPa)	0.4	0.4	0.4	0.4
Particle radius (m)	1.5	1.5	1.5	1.5
Friction angle (talus)	45°	45°	45°	45°
Friction angle (core)	0	0	0	0
Cohesion for ductile core (MPa)	0.2	10	0.2	10
Parallel bond stiffness ( $N/m^3$ )	$1 \times 10^6$	$1 \times 10^8$	$1 \times 10^6$	$1 \times 10^8$
Linear contact stiffness (N/m) (ductile core)	$5 \times 10^8$	$5 \times 10^8$	$5 \times 10^8$	$5 \times 10^8$
Linear contact stiffness (N/m) (talus)	$2.25 \times 10^9$	$2.25 \times 10^9$	$2.25 \times 10^9$	$2.25 \times 10^9$
Yield strength of parallel bonded material (MPa)	0.2	5	0.2	5
Young's modulus (talus without parallel bond) (GPa)	3	3	3	3

transition to a liquid state. Upon crystallization the magma develops mechanical strength appropriate to that of lava blocks, i.e. talus. This is a simplified assumption as in some cases we recognize that the lava may not be broken up in this fashion. The empirical expression for the solidus pressure isobar is used to dynamically identify the interface between the viscous/cohesive core and frictional talus in the model lava dome during its evolution – although the frictional rind may develop thickness variations by accumulation, mixing, sliding or overplating of previously solidified particles. The properties of the model lava dome are updated after every time step. Experiments performed on Soufrière Hills lavas are used to constrain the variables that include pressure, temperature and water content; the temperatures for the magma range from 830 °C to 940 °C (Barclay et al., 1998; Rutherford and Devine, 2003) and solidus pressure lies between 0.1 and 5 MPa as shown in Fig. 4 (Hale, 2008).

Identification of the ductile core-solidified lava interface within the model domain allows the material properties to be updated. Studies conducted to obtain the value of the macroscopic magnitudes of cohesion and coefficient of friction include back analysis of failure (Simmons et al., 2005). The broad range of pairs for cohesion and friction angle pair obtained from back analysis vary from 0 to 1.1 MPa and from 0 to 45° which cover the rheologic range of viscous magma through solidified lava. This covers the approximate range of material strength for major collapse events that occur at slow to moderate extrusion rates. Idealized material properties of the core and talus are given in Table 4. Frictional parameters of SHV lava have been determined in the laboratory (Voight et al., 2002; Samuelson et al., 2008).

### 3. Parametric sensitivities

Discrete element model (DEM) simulations track both spatial and temporal evolution of idealized lava dome growth. The model is parameterized with values of mechanical properties taken as representative of Soufrière Hills Volcano (SHV). Parametric analyses are performed to explore the sensitivity of the patterns of lava dome growth to parameter selections. Ranges of selected values for flow rate, material stiffness, coefficient of friction and cohesion considered appropriate for SHV are given in Table 4. Specifically, these material variables represent stiffness, friction and cohesion and together with extrusion rate influence the morphology of the evolving dome.

#### 3.1. Material stiffness

In these analyses, the particle radius representing discrete packets of magma is 1.5 m with the material stiffness of the particle indicative of its compressibility. For particles representing a slightly compressible continuum the normal ( $k_n$ ) and shear ( $k_s$ ) stiffnesses of two cylindrical particles in contact are correlated to Young's ( $E$ ) and shear ( $G$ ) moduli by Eqs. (4) and (5) respectively. The dependence of stiffness of the parallel bond to Young's modulus ( $E$ ) is expressed in Eq. (9). As discussed above, the bulk material properties vary with temperature and pressure along the path of magma ascent. The magma ascent rate significantly

influences crystal nucleation, crystal growth rate and the exsolution of volatiles (Hort, 1998; Melnik and Sparks, 1999; Martel and Schmidt, 2003; Melnik and Sparks, 2005; Blundy et al., 2006) and compressibility of the magma is in turn affected by this volatile content (Huppert and Woods, 2002; Woods and Huppert, 2003). A lower material stiffness at higher flow rates is a consequence of the higher retained volatile content that in turn significantly increases magma compressibility (Cashman and Blundy, 2000; Woods and Huppert, 2003). Magma stiffness is reasonably well constrained and the modulus of the dome core is an order of magnitude lower than that of the talus (see Table 4) (Voight and Elsworth, 1997; Elsworth and Voight, 2001; Hale and Wadge, 2003; Widwijayanti et al., 2005; Sporli and Rowland, 2006).

Material stiffness affects the morphology of the lava dome that evolves in our particulate model, resisting deformation by the creation of "force chain networks" (Estep and Dufek, 2013). The force chain network is a string of particles in contact with each other that resist deformation in a granular aggregate, controlling macroscopic characteristics and affecting the transport capacity of granular flows. Fig. 5 shows the effect of stiffness on the morphology of a growing endogenous lava dome. Changes in assumed stiffness change the shape of the core as apparent in Fig. 5. The height of the evolving dome increases with an increase in stiffness (lava dome height is 62 m for the stiffer magma with a linear contact stiffness of  $7.5 \times 10^9$  N/m, while for the less stiff magma with a linear contact stiffness of  $2.25 \times 10^9$  N/m the height is 55 m) of the injected magma due to the enhanced resistance of the bulk material to compression/compaction. Dome core growth concentrates above the center of the conduit when magma stiffness is high, whereas lateral spreading is promoted when stiffness is low (Fig. 5). The dome structure observed for magma of low stiffness is similar to the reported experimental results obtained for flow of silica gel between parallel plates which directs the fluid onto a rigid horizontal base (Buisson and Merle, 2002).

The variation of material stiffness in the simulation is analogous to viscosity in the case of endogenous growth. As viscosity increases, the growth of the core concentrates above the conduit (Hale, 2008). Similarly, in our models, where viscosity is not explicitly incorporated, a higher material stiffness (core height is 47 m for the stiffer magma with parallel bond stiffness of  $1 \times 10^8$  N/m<sup>3</sup>, while core height is 40 m for the less stiff magma with a parallel bond stiffness of  $1 \times 10^6$  N/m<sup>3</sup>) during endogenous growth results in a core with greater height, while models with reduced stiffness the relative lateral spreading is increased.

#### 3.2. Coefficient of friction

In general, talus surrounding the lava dome acts as a constricting particulate shell constraining the softer material of the dome core. The force exerted between talus particles is a function of the coefficient of friction of the material, modulated by the local contact force. In our models, the talus naturally evolves to enclose the soft dome core and forms an apron that surrounds the outer structure of the lava dome. The greater the coefficient of friction, the higher the constricting force exerted on the core by the talus around the base of the dome (lava

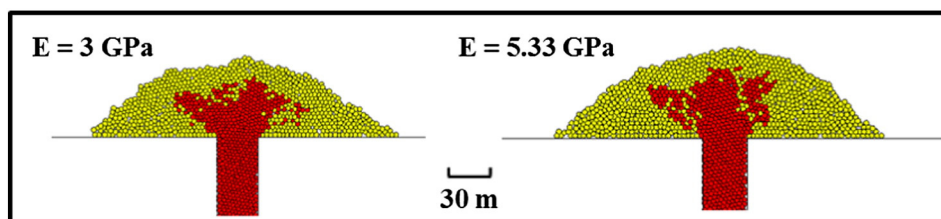
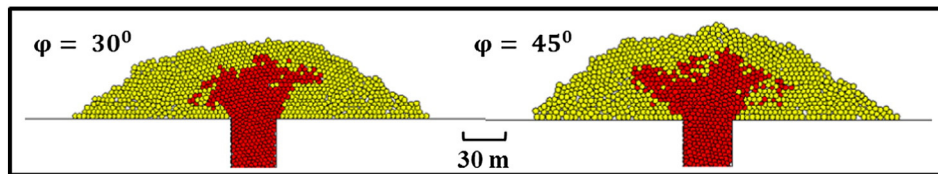


Fig. 5. Variation in lava dome morphology due to change in material stiffness which is evolving on injection at a constant flow rate of 5 m<sup>3</sup>/s as the lava dome evolves over a time period of  $\approx 14$  h (material properties given in Table 3) (red particles indicate core material and solidified lava is represented by yellow particles). (For interpretation of the references to color in this figure legend, the reader is referred to the web version of this article.)



**Fig. 6.** Variation in lava dome morphology due to change in internal friction angle of the talus evolving from ductile core material on injection of magma at a constant flow rate of  $5 \text{ m}^3/\text{s}$  as the lava dome evolves over a time period of  $\approx 17.5 \text{ h}$  (material properties given in Table 3).

dome height for the talus with  $\phi = 30^\circ$  is 52 m, while the lava dome height for the talus with a friction angle of  $45^\circ$  is 55 m). Simulations using two limiting values ( $\phi = 30^\circ$  and  $45^\circ$ ) for the angle of internal friction (e.g. Samuelson et al., 2008) give similar morphologies for the resulting dome with a marginal difference in the lava dome height, although the coefficient of friction does influence the internal structure of the core during endogenous growth. The higher the coefficient of friction, the greater the lateral confining force, and the greater restriction to lateral spreading of the magma core (lava dome core radius and height for  $\phi = 45^\circ$  is 90 m and 45 m respectively, while for  $\phi = 30^\circ$  the radius and height are 87 m and 40 m respectively) (Fig. 6). The effect of friction angle is most prominent for domes of greater height-to-radius ratio. Rationally, the angle of repose of the talus is greater for talus with greater friction angle (e.g. Hale, 2008). In a constantly evolving lava dome the coefficient of friction does not appear to have a significant influence on its final morphology.

### 3.3. Cohesion

Degassing-induced crystallization increases the viscosity of the magma (Hammer et al., 2000) and adds strength, reflecting non-Newtonian magma behavior (Blake, 1990; Sparks, 1997; Voight et al., 2002; Melnik and Sparks, 2005; Lavallee et al., 2007), when the closure/solidus pressure is approached. Rates of strength gain for dominantly frictional material (talus) or frictional plus strongly cohesive material (unfragmented carapace) are not well constrained. Back analyses of collapsed lava domes provide estimates of cohesion and friction angles (Simmons et al., 2005). Estimates for bulk material cohesion for endogenous domes range from 0.1 to 1.1 MPa, while the strength estimates for a viscous plug in the simulation are an order of magnitude higher than that for endogenous growth. Spines are assumed to behave

as a cohesive material, and have a maximum height that is controlled by strength. In reality this simple relationship is more complex as the bulk strength of the spine material continuously varies with cooling, degassing, fracturing and rain-water infiltration, as a function of growth rate and spine morphology and is heterogeneously distributed over the volume of the spine (Voight, 2000).

The rheology of degassed crystalline lava is complex and an approximation used to describe the non-Newtonian behavior is the Bingham flow law. The apparent and actual viscosity will differ for a fluid with finite yield strength (Blake, 1990; Lejeune and Richet, 1995; Griffiths, 2000; Caricchi et al., 2007). The apparent viscosity of the crystal rich lava can be higher than  $10^{13} \text{ Pa s}$  with a yield strength of more than 1 MPa (Voight et al., 1999; Voight, 2000). The simulation runs for lava with a material strength (equivalent to parallel bond strength) of 0.5 MPa and 2 MPa at a constant flow rate of  $2 \text{ m}^3/\text{s}$  are represented by points c and d in Fig. 7. The total erupted volume for the simulation run is  $212,155 \text{ m}^3$  ( $t = 29.5 \text{ h}$ ). At the start of the eruption cycle, magma with lower material strength (0.5 MPa) extrudes for the initial 20 h ( $141,500 \text{ m}^3$ ). Table 4 gives the remaining material properties used for the simulation. The modeled lava dome evolves endogenously during this period. Point c represents the endogenous lava dome structure (dome height 35 m and radius 76.5 m, ductile core height 26 m and radius 31.5 m) after the eruption of  $106,100 \text{ m}^3$  ( $t = 14.75 \text{ h}$ ). At the end of the first 20 h of eruption, a higher material stiffness and material strength (2 MPa) is assigned to the particles assuming an increase in crystal fraction and lower magma volatile and melt content. The material with greater strength and therefore greater parallel bond stiffness is able to punch through the material overlying the conduit exit resulting in exogenous growth. Point d represents the transition in flow pattern from endogenous to exogenous dome growth of a fragmented lava lobe ( $t = 29.5 \text{ h}$ ). The effect of variable material

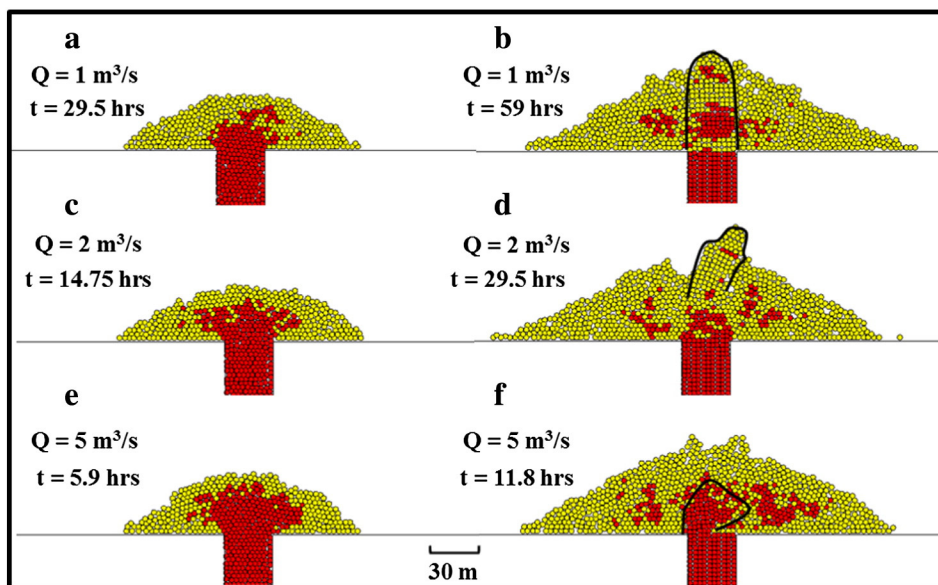


**Fig. 7.** Modeled lava dome structures for three different discharge rates ( $1 \text{ m}^3/\text{s}$ ,  $2 \text{ m}^3/\text{s}$  and  $5 \text{ m}^3/\text{s}$ ) for a total volumetric eruption of  $212,155 \text{ m}^3$ . Material strength of the erupting lava is varied from 0.5 MPa to 2 MPa after a volumetric eruption of  $141,500 \text{ m}^3$ . The snapshots at points a, c, d are taken after a volumetric eruption of  $106,100 \text{ m}^3$  and b, d, f are the modeled lava dome structures at the end of the simulation run.

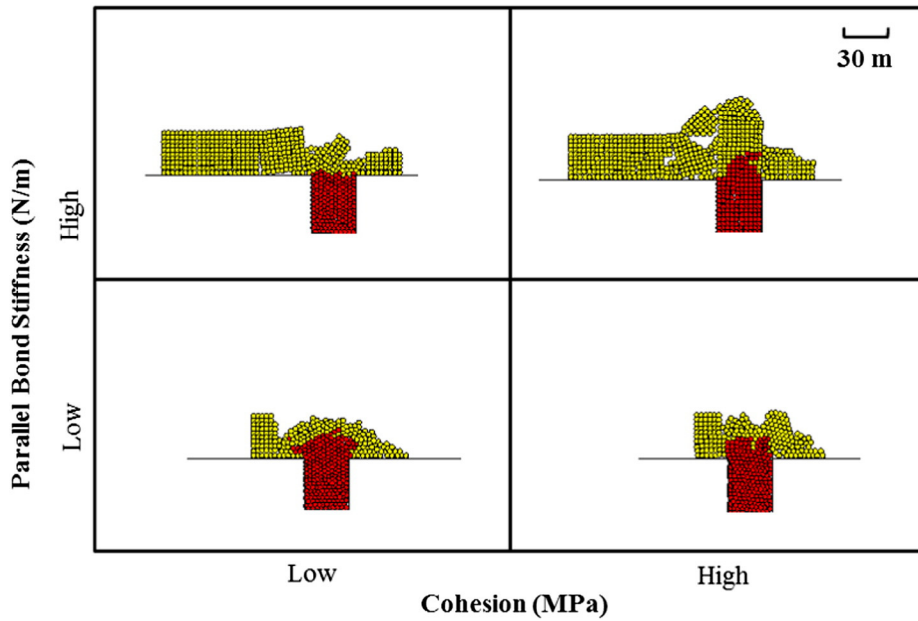


**Fig. 8.** Effect of parallel bond stiffness and cohesion on the simulated morphology of the modeled magma particles for a total volume of  $V = 114,000 \text{ m}^3$  for high stiffness material and  $V = 46,400 \text{ m}^3$  for low stiffness material at a constant flow rate of  $Q = 0.5 \text{ m}^3/\text{s}$  or flow velocity  $\approx 7.07 \times 10^{-4} \text{ m/s}$  in the PFC<sup>2D</sup> model.

strength on the morphology of the lava dome is discussed in detail in Section 4 and represented in Figs. 8–11.

3.4. Extrusion rate

As noted previously, the solidification of lava follows two different mechanisms: cooling and degassing. Both result in rheological stiffening that is driven by degassing-induced crystallization. Degassing-induced crystallization is the dominant mechanism for rheological stiffening of intermediate composition lavas, as conductive cooling penetrates too slowly to be effective on the short time-scales (Sparks et al., 2000; Hale, 2008). The extrusion rate affects the texture of the extruded lava varying significantly with paths of temperature and pressure. Crystallization results in large changes in viscosity, and at threshold crystal

content, magma develops non-Newtonian properties and mechanical strength (Sparks et al., 2000; Petford, 2003). In addition, the process of gas escape affects the pressure of volcanic flow and magma ascent rates (Jaupart, 1998; Diller et al., 2006; de Michieli Vitturi et al., 2010).

At lower extrusion rates, gas loss is promoted (Diller et al., 2006) and crystallization reaches a critical crystal content which leads to the development of mechanical strength by crystal locking (Innocenti et al., 2013a,b). Thus, the material experiences a transition from a viscous Newtonian to a non-Newtonian fluid with a Bingham-like yield strength. At higher extrusion rates gas loss is diminished and the volatile content of the magma is greater, resulting in relatively low viscosity magma. The variable properties of lava associated with variable extrusion rate and gas loss results in distinctive variations in the morphologies and growth patterns of natural domes (Watts et al., 2002).

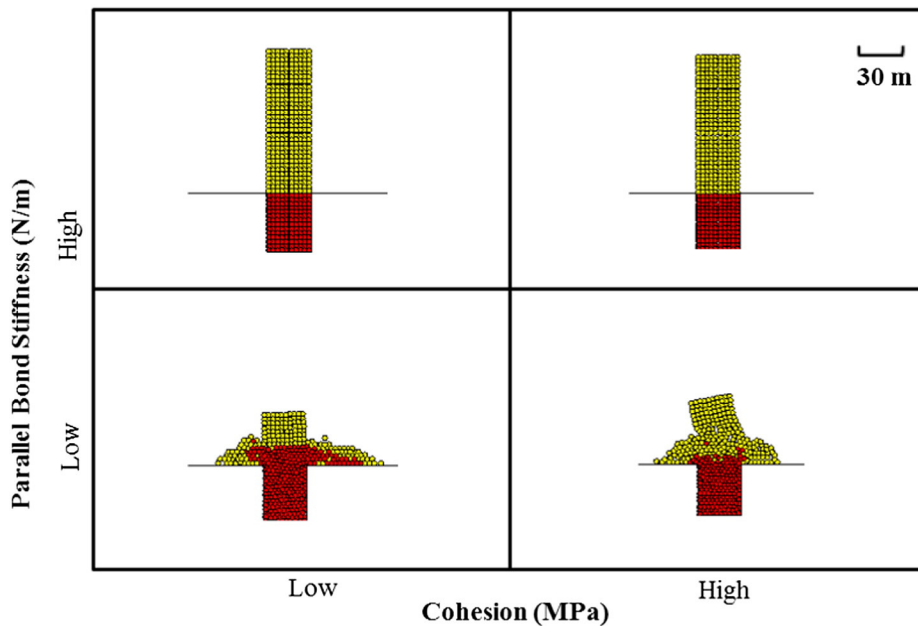


**Fig. 9.** Effect of parallel bond stiffness and cohesion on the simulated morphology of the modeled magma particles for a total volume of  $V = 55,000 \text{ m}^3$  for high stiffness material and  $V = 45,000 \text{ m}^3$  for low stiffness material at a constant flow rate ( $Q = 10 \text{ m}^3/\text{s}$  or flow velocity  $\approx 1.414 \times 10^{-2} \text{ m/s}$  in the PFC<sup>2D</sup> model).

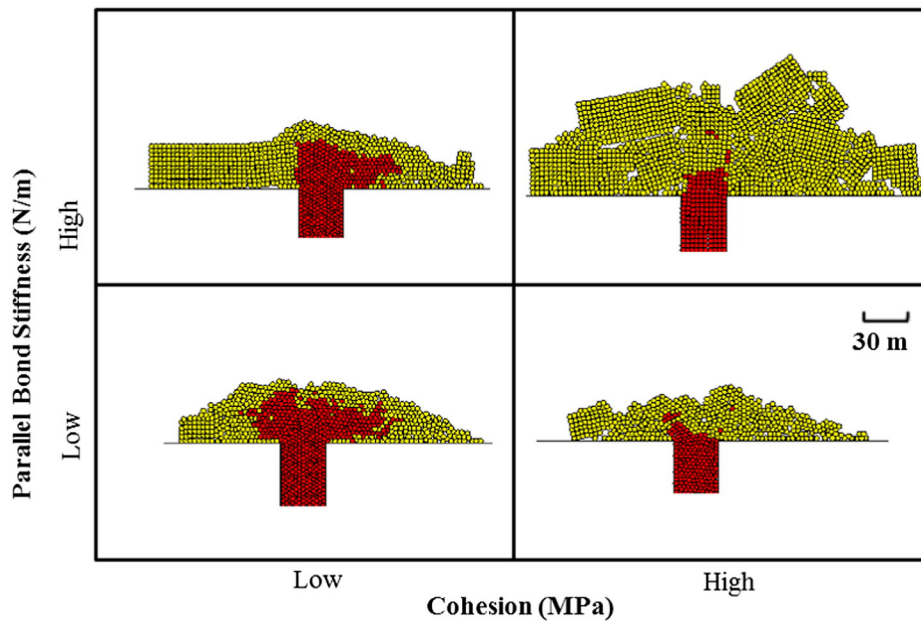


**Fig. 10.** Effect of parallel bond stiffness and cohesion on the simulated morphology of a lava dome with a maximum external radius of 100 m and developing at a constant flow rate ( $Q = 0.5 \text{ m}^3/\text{s}$  or flow velocity  $\approx 7.07 \times 10^{-4} \text{ m/s}$  in the PFC<sup>2D</sup> model) (total volume of the simulated lava dome varies for each simulation as the height of the evolving dome is different).

Points a–f in Fig. 7 represent the results for 3 model runs with different extrusion rates ( $1 \text{ m}^3/\text{s}$ ,  $2 \text{ m}^3/\text{s}$  and  $5 \text{ m}^3/\text{s}$ ). The material stiffness and strength is varied from 0.5 MPa to 2 MPa after the eruption of a simulated volume of  $141,500 \text{ m}^3$ . The simulation run is stopped after a total erupted lava volume of  $212,155 \text{ m}^3$ . The other material properties are maintained as given in Table 4. Point e represents the endogenous lava dome structure evolving at a constant flow rate of  $5 \text{ m}^3/\text{s}$  for an erupted volume of  $106,100 \text{ m}^3$  ( $t = 5.9 \text{ h}$ ). It is observed that for the same erupted volume, the maximum height of the dome increases for increasing extrusion rate. The maximum heights of the simulated lava dome for the 3 different extrusion rates ( $1 \text{ m}^3/\text{s}$ ,  $2 \text{ m}^3/\text{s}$ ,  $5 \text{ m}^3/\text{s}$ ) shown in Fig. 7 by points a, c and e are 35 m, 36 m and 39 m respectively. The increase in extrusion rate increases the pressure at the conduit exit

that balances the overburden pressure due to the lava dome height (Hale, 2008). The dome structure at point a ( $t = 29.5 \text{ h}$ ) is representative of the conceptual sketch of a mature lava dome evolving endogenously, while point e ( $t = 5.9 \text{ h}$ ) represents the conceptual shape of a juvenile dome (see Figure 6d in Buisson and Merle, 2002). The dome growth for point e is dominated by vertical growth due to higher extrusion rate, as the growth rate of dome height decreases as the modeled dome spreads laterally and growth is gravity driven as observed at point a (Hale et al., 2007). For the lowest flow rate ( $1 \text{ m}^3/\text{s}$ ) the growth of the ductile core is concentrated around the conduit exit (height 24 m and radius 21.5 m) as the region of the dome at pressures above the solidus pressure is smaller (Fig. 7a). At higher flow rates ( $5 \text{ m}^3/\text{s}$ ) the region of the dome at pressures above the solidus is larger and therefore

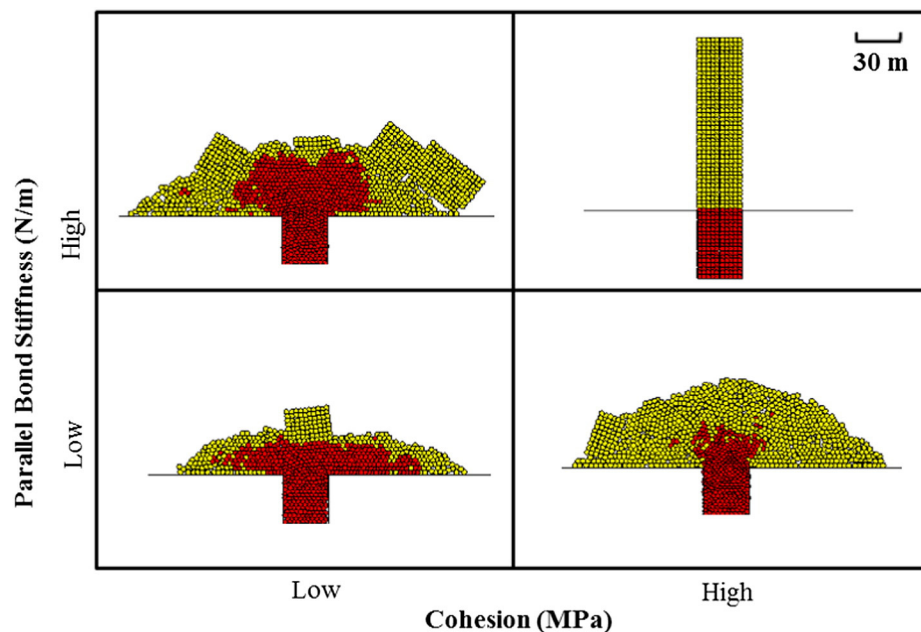


**Fig. 11.** Effect of parallel bond stiffness and cohesion on the simulated morphology of a lava dome with a maximum external radius of 100 m and developing at a constant flow rate ( $Q = 10 \text{ m}^3/\text{s}$  or flow velocity  $\approx 1.414 \times 10^{-2} \text{ m/s}$  in the PFC<sup>2D</sup> model) (total volume of the simulated lava dome varies for each simulation as the height of the evolving dome is different).

the percentage volume of the ductile core is higher (height 32 m and radius 31 m) (Fig. 7e).

The endogenous regime of growth is mostly interrupted by the direct extrusion of lava directly to the surface of the lava dome (Hale and Wadge, 2008). An increase in the crystallinity of the magma results in an increase in effective viscosity with this effect accommodated in the later part of the 3 model runs by increasing the material stiffness and strength. The material stiffness and strength of the ductile core is varied to  $1 \times 10^8$  N/m<sup>3</sup> and 2 MPa respectively. A solid degassed crystallized lava plug develops in the dome close to the conduit exit at the lower flow rates (1 m<sup>3</sup>/s) as the region in the modeled dome at pressures above solidus pressures is smaller. This stiffer solid lava plug punches to the surface as shown at point b (total erupted volume 212,155 m<sup>3</sup> at  $t = 11.8$  h). At higher flow rates (5 m<sup>3</sup>/s) the growth of an endogenous lava lobe is observed as a larger region of the dome is at pressures above the solidus. Point e represents the growth of the lava lobe after a total volumetric eruption of 212,155 m<sup>3</sup> ( $t = 59$  h). The simulation results represented by points a–f show that a larger ductile core develops at higher flow rates (5 m<sup>3</sup>/s) for material with lower material stiffness and strength (0.5 MPa), while at lower flow rates (1 m<sup>3</sup>/s) the flow pattern changes to exogenous growth for material with greater material stiffness and strength (2 MPa). The variation in dome morphology and magma rheology is discussed in detail in the following section for the end member values of extrusion rates (low flow rate 0.5 m<sup>3</sup>/s and high flow rate 10 m<sup>3</sup>/s) observed at Soufriere Hills Volcano, Montserrat (1995–1999).

#### 4. Models of dome evolution

We evaluate the variation in dome morphology and magma rheology for the range of extrusion rates observed at Soufrière Hills Volcano, Montserrat (Sparks et al., 1998; Watts et al., 2002; Wadge et al., 2010). As discussed above, the extrusion rate significantly affects the material properties of the extruded lava. The different lava dome morphologies that are observed result from this important interplay between the extrusion rate and dome material properties. Table 4 illustrates the range of material properties and flow conditions used for the various simulations. Simulations vary from relatively low to high extrusion rates ( $Q = 0.5$  m<sup>3</sup>/s for Figs. 7 and 9,  $Q = 10$  m<sup>3</sup>/s for Figs. 8 and 10) assuming material properties with variable cohesion and material stiffness.

Resulting dome morphologies for the range of parameters are given in Figs. 8–11. The linear contact bond stiffness and friction angle for the modeled carapace/talus material (yellow particles) is maintained constant for all simulations, while parallel bond stiffness and bond strength are varied for the ductile core (red particles). The total volume extruded for the simulation runs in Fig. 8 for material with high stiffness is ~114,000 m<sup>3</sup> and for low stiffness is ~46,400 m<sup>3</sup>, while the extruded volume in Fig. 9 for high stiffness material is ~55,000 m<sup>3</sup> and low stiffness is ~45,000 m<sup>3</sup>. The total volume extruded in the simulations for high stiffness material in Fig. 8 is higher as the time needed for the more viscous magma to manifest a change in its flow pattern at the assumed low flow rate required a higher erupted volume. Material properties assigned to the particles in simulation runs for Fig. 10 are the same as those assigned in Fig. 8, while the properties used in Fig. 11 match the values used for Fig. 9. The simulations in Figs. 10 and 11 were terminated when the modeled lava dome grew to a radius of 100 m, yielding different total volumes in the simulations. The total volume for simulation run in Figs. 10 and 11 varies for each simulation run as observed for the simulation for high stiffness/high cohesion material. This material behaves analogous to a highly viscous magma that tends to accumulate around the conduit exit which leads to the formation of a lava dome with a significantly higher ratio for the height to radius of the simulated lava dome. As a result the total erupted volume for high stiffness/high cohesion material is greater as compared to the other simulation runs (Fig. 10).

The properties assigned to the particles for the compressional (linear contact) and parallel bonds (Fig. 8–11) are influenced by the extrusion rate considered for the simulation run. At lower extrusion rates ( $Q = 0.5$  m<sup>3</sup>/s) (Figs. 8 and 10) the volume percentages of volatile and melt content are lower, and this results in elevated material stiffnesses and reduced deformation. Higher parallel bond stiffness and bond strength are assigned to the modeled particles in the simulations with low flow rate. The effective Young's modulus ( $E$ ) of the modeled particle assemblage (where a parallel bond exists between particle–particle contacts) is a function of compressional bond stiffness and parallel bond stiffness. A parallel bond exists for all modeled ductile core particle–particle interactions. The effective Young's modulus ( $E$ ) for the modeled ductile core and carapace (with an active parallel bond between interacting particles) is given by Eq. (9). The effect of parallel bond stiffness on effective Young's modulus ( $E$ ) increases as the difference between the magnitudes of  $k_n$  and  $k^n$  decreases (for example, cases represented by High–High in Figs. 8–11). The modeled carapace material breaks to form talus at the margins of the modeled lava dome when the applied stress exceeds the bond strength which is given by Eqs. (7) and (8).

Fig. 8 shows the effects of variation of parallel bond stiffness with cohesion at low flow rates ( $Q = 0.5$  m<sup>3</sup>/s) (Table 4). At these low flow rates blocky growth results for magma with higher bond stiffness, while lower bond stiffness and lower bond strength results in larger deformation (visually more ductile). The parallel bonds are broken at the higher flow rate (Fig. 9 and  $Q = 10$  m<sup>3</sup>/s) for material with lower parallel bond stiffness and bond strength. This causes a slight reduction in the effective Young's modulus and results in relatively greater deformation/damage. Parallel bonds regulate sliding between interacting particles. A broken parallel bond is not regenerated, which leads to an increase in particle sliding and overall deformation. A similar trend is observed in Fig. 10 for the material with high parallel bond stiffness and low cohesion extruded at a constant rate ( $Q = 0.5$  m<sup>3</sup>/s).

In all simulations (Figs. 8 to 11), a lava lobe is generated at the initiation of the eruption (defined as a minimum volume of  $\approx 25,000$  m<sup>3</sup> for all simulations). The growth of this lava lobe depends on the contact bond stiffness, parallel bond stiffness and cohesion of the particles. A higher parallel bond stiffness ( $k^n = 1 \times 10^8$  N/m<sup>3</sup>) and greater cohesion (10 MPa) principally generates a vertical extrusion above the conduit (Figs. 9 and 11). Subsequent dome growth after the initial collapse of the extrusion is controlled by the parallel bond stiffness and cohesion. Differences in the morphologies of dome growth are most pronounced after a significant release of conduit magma which reveals contrasting internal flow patterns of magma in the dome.

Flow patterns transition to endogenous growth after spine collapse in material with low stiffness and low cohesion. This behavior is apparent in Figs. 9 and 11, but is less evident in Figs. 8 and 10. It is represented and discussed in more detail in Sections 5.1 and 5.2. The change in flow pattern of the particle assemblage occurs upon the breakage of parallel bonds, which in turn results in the reduction of the bulk modulus. Material stiffness at low extrusion rates ( $Q = 0.5$  m<sup>3</sup>/s) varies from 3 to 30 GPa (Widiwijayanti et al., 2005). Material with low parallel bond stiffness and low cohesion is not capable of punching through the overlying material above the conduit exit (Figs. 8 and 10). The observed growth of a spine occurs only at low extrusion rates and requires a material with both greater parallel bond stiffness and high material strength (Fig. 10 – collapsed blocky lava surrounding the conduit exit). A lower dissolved magma volatile content implies that the bulk compressibility of the material is low, resulting in less deformation and higher material stiffness. At lower flow rates a higher material stiffness and material strength is assigned to the particles as a direct result of increased crystal fraction, lower magma volatile and melt content (Table 4) that results in reduced deformation. A material with greater strength and parallel bond stiffness is able to punch through the material overlying the conduit exit resulting in the generation and protrusion of a spine. Conversely, material with lower stiffness and strength (which is assigned at higher flow rates) results in endogenous growth (Figs. 10 and 11) and no spine.

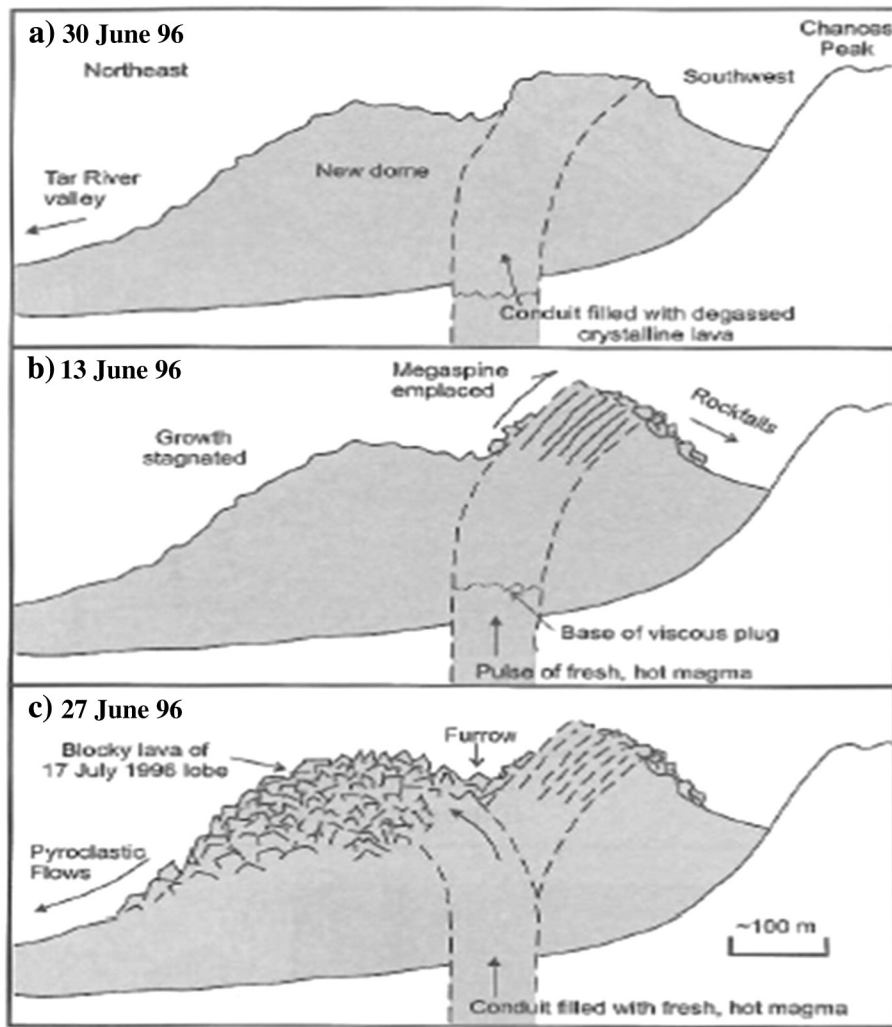


**Fig. 12.** Switching activity and emplacement of the megaspine in June and July, 1996 at Soufrière Hills Volcano, Montserrat illustrated in a cross-sectional (X–Y) diagram. (a) Period of slow growth (30th June, 1996) with rockfall at the summit and formation of a solid magma plug. (b) Emplacement of the plug as a megaspine, along the curved shear fault within the dome which occurs due to the infusion of fresh magma through the conduit (13th July, 1996). (c) Rapid rise of hot magma along an alternative shear fault acts as an easier way for the magma to reach the surface. The rapid rise does not allow a plug to form leading to the development of a shear lobe comprising large blocks and stubby spines (Watts et al., 2002).

At higher extrusion rates ( $Q = 10 \text{ m}^3/\text{s}$ ) the material contains more volatiles (high melt fraction) resulting in higher compressibility. At extrusion rates above  $2\text{--}3 \text{ m}^3/\text{s}$  lava dome growth is endogenous with a cohesive core and frictional carapace. Hence, a material with low parallel bond stiffness and low cohesion leads to endogenous growth at high flow rates (Figs. 9 and 11). The range of material cohesion for the core is in agreement with the values obtained in back calculations (Simmons et al., 2005). Thus endogenous growth results at higher flow rates for material with low stiffness and low material strength. The morphology of the evolving domes (Figs. 8 to 11) differ significantly and this is governed by the parallel bond stiffness, cohesion and extrusion rate considered.

## 5. Mechanistic interpretation of dome growth at Soufrière Hills Volcano, Montserrat

We use the granular mechanics model described above to provide insights into mechanisms of lava dome growth and collapse. We compare observations of lava dome growth at SHV, Montserrat with our simulations, and focus particularly on the lava dome growth period from June to July, 1996. Dome growth during this period at SHV was dominated by the evolution of fault-bounded megaspines (Fig. 12a and b). Megaspines comprise a lava monolith extruded along a smooth

striated curving fault and bounded on its opposing face by blocky lava (Fig. 12c) (Watts et al., 2002). Emplacement of these structures occurred over several days, subsequently followed by renewed activity localized elsewhere in the dome. In particular the following describes necessary conditions for the extrusion of spines and the resulting dependence of dome morphology on extrusion rate.

### 5.1. Controls on spine evolution

We examine this behavior using the flow history of Fig. 13. Lava dome growth during the period (June–July, 1996) was observed to vary between  $1$  and  $4 \text{ m}^3/\text{s}$  (Melnik and Sparks, 2002; Watts et al., 2002). The flow-rate history assumed in our simulations was selected to represent the observed change in flow pattern and its effect on the modeled lava dome morphology (and to minimize simulation run time). Simulation flow-rate history is shown in Fig. 13, with the corresponding evolution of the model at specific times shown in Fig. 14. At the start of the eruption cycle ( $t = 0 \text{ h}$ ) the lava extrudes vertically above the vertical conduit as no resistance is offered to flow in the absence of overlying material. The extruded lava then begins to collapse ( $t = 2.5 \text{ h}$ ) under the weight of the overlying column (Fig. 14I). Upon this initial collapse the flow pattern changes to endogenous dome growth. Thus our simulation of the modeled lava dome is initiated by

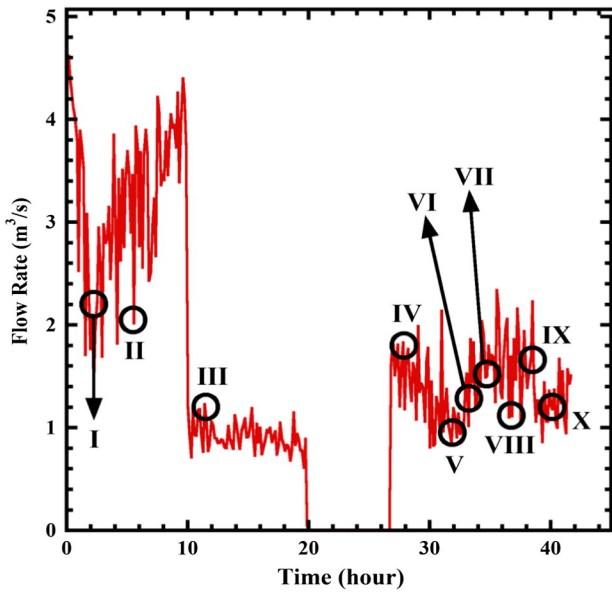


**Fig. 13.** Flow-rate history assumed to model a simulated lava dome eruption illustrating different growth patterns observed at Soufriere Hills Volcano, Montserrat during June to July, 1996. Snapshots of the modeled morphology are taken at points labeled from I to X.

initiating endogenous dome growth at an average flow rate of  $\sim 3 \text{ m}^3/\text{s}$  (e.g. Fig. 14II where  $t = 5.5 \text{ h}$ ) for the first 10 h (Fig. 13). The flow rate is then reduced to  $\sim 1 \text{ m}^3/\text{s}$  for the subsequent 10 h. Given that magma

**Table 5a**

Parameter value considered for model run for the eruption cycle given by Fig. 13.

Period of eruption	Parallel bond stiffness (N/m <sup>3</sup> )	Cohesion (MPa)	Pseudo/effective viscosity (Pa·s)
Initiation–point II	$1 \times 10^6$	0.4	$1.5 \times 10^6$
Point III	$1 \times 10^7$	10	$3 \times 10^7$
Points IV–X	$3 \times 10^6$	10	$9 \times 10^6$

crystallization increases at the lower flow rate, the material stiffens (Table 5a). The lava dome structure after  $\sim 11.4 \text{ h}$  of simulated eruption is given by point III in Fig. 14. After 20 h, we stop extrusion of lava for  $\sim 6.7 \text{ h}$ . During this period of stagnation the magma in the conduit crystallizes and degasses to form a plug, with resulting increases in strength and stiffness. The increase in material stiffness and strength of the magma due to degassing-induced crystallization is represented by an increment in parallel bond stiffness and material strength (cohesion) of the model particles in the conduit (Table 5a). During the period of stagnation in the simulation, the modeled lava dome structure does not experience significant gravitational relaxation due to the short time period. Thus the morphology of the lava dome remains essentially constant. The flow of magma is re-invigorated at time IV (Fig. 14) and the structure of the simulated lava plug resembles the form interpreted for 30th June, 1996 and shown by Fig. 12a. The crystalline degassed lava plug is then extruded by the pulse of fresh magma producing a megaspine as shown in Fig. 14V and VI and is representative of the structure observed for 13th July, 1996 shown in Fig. 12b (Watts et al., 2002).

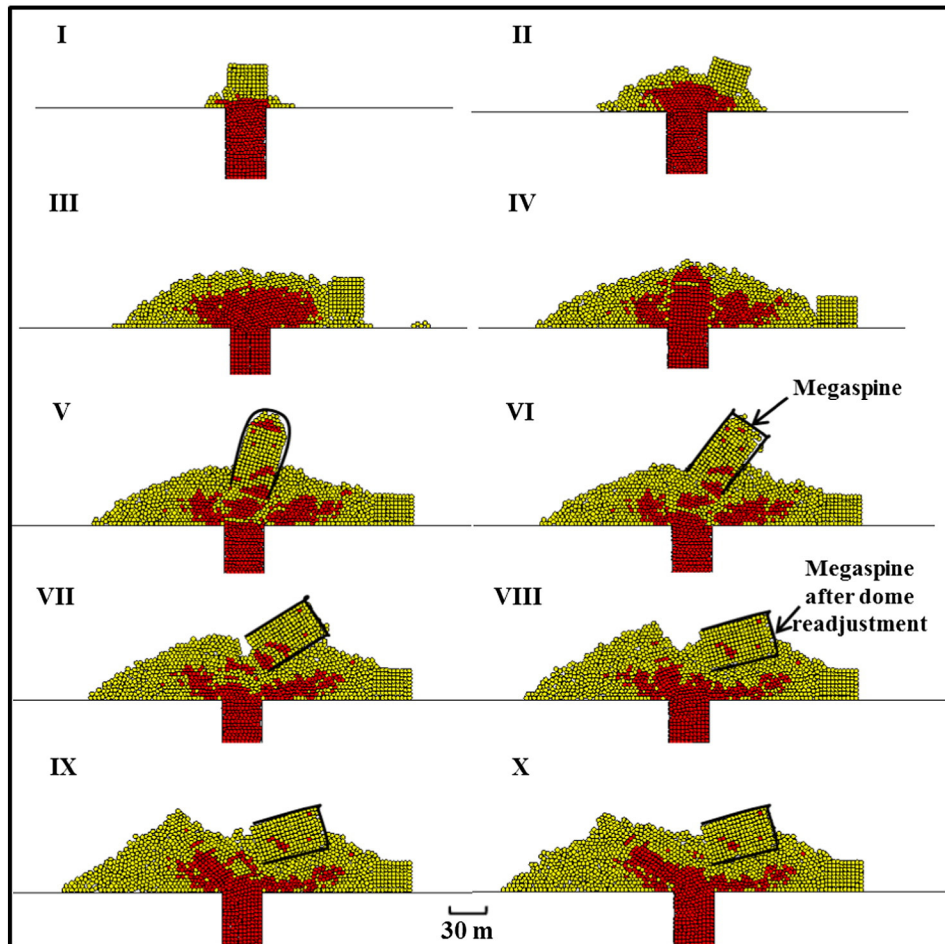


**Fig. 14.** Lava dome morphology variation with flow rate to replicate with reasonable approximation the mechanistic behavior of the growth pattern observed during lava dome evolution from June to July, 1996 at Soufrière Hills Volcano, Montserrat.

Emplacement of a megaspine at SHV was observed to stop after a few days and eruptive activity renewed in another localized part of the dome. Vigorous spurts of fresh lava at higher extrusion rates ( $>5 \text{ m}^3/\text{s}$ ) were redirected along shear faults in a specific direction away from the previous growth area (Watts et al., 2002). A similar mechanistic behavior is observed in Fig. 13VIII–X, where the buildup in resistance to movement by the emplaced megaspine triggers the re-direction of magma flow to create a new shear fault and the dome then grows in a different direction. The injection of fresh magma into the dome resulted in the readjustment of the simulated dome structure that caused the lateral spreading of the blocky lava. The reinvigoration of magma flow leads to a change in the position (away from the conduit exit) of the emplaced monolithic structure (Fig. 13VI–VII) in the simulation; while as observed at SHV, the position of the emplaced megaspine remained constant for a year before being bulldozed by a northward growing shear lobe. During this period the magma plug grows in almost the opposite direction, with blocky lava developing at the topmost part of the magma plug. Similar characteristics are also evident in the evolution of lava domes on Montserrat (Watts et al., 2002; Tuffen and Dingwell, 2005; Loughlin et al., 2010; Ryan et al., 2010) and at Mt St. Helens during the 2004–2006 eruption (Cashman et al., 2008).

The transition from endogenous to exogenous growth is significantly influenced by the crystallinity of the extruding magma. The model focuses on the effect of material strength on magma rheology resulting in the variation of lava dome morphology. The crystallinity of the lava extruded at the free surface of the Soufriere Hills Volcano, Montserrat is observed to be up to 90%. A comprehensive comparison with the experimental data from Couch et al. (2003) is given by Melnik and Sparks (2005). In the study the calculated crystal fraction content at the conduit exit varied between  $\sim 0.9$  and  $\sim 0.62$  for magma ascending at a constant flow rate of  $0.32 \text{ m}^3/\text{s}$  and  $8.1 \text{ m}^3/\text{s}$  respectively, with initial crystal fraction content of 0.6 at a depth of 5000 m with conduit radius of 15 m and initial volatile content of 5 wt.%. The time taken by the magma ascending at a flow rate of  $0.32 \text{ m}^3/\text{s}$  and  $8.1 \text{ m}^3/\text{s}$  to reach the conduit exit is 128 days and 5 days, respectively. Results obtained from 3-D models of crystal networks suggest that the range for maximum crystal volume fraction beyond which the magma behaves as a brittle solid varies between 0.74 and 0.8 (Saar et al., 2001; Hale, 2007). Observational data suggest that for the extrusion of lava structures at Soufriere Hills

Volcano, Montserrat with shear surfaces that exhibit solid-like deformation requires a crystal volume fraction greater than 0.7 (Watts et al., 2002). Thus the transition in lava dome growth pattern from endogenous growth (magma with low crystal content) to exogenous growth (highly crystallized lava) would lie between 5 days and 128 days after the initiation of eruptive activity. The study by Hale and Wadge (2008) with similar initial conditions graphically represents the compatible combination of extrusion rate and magma crystallinity required for the initiation of exogenous dome growth. Observational data from the numerical experiment in the study conducted to simulate the eruptive activity at Soufriere Hills Volcano, Montserrat (October–December, 1996) suggest that transition from endogenous to exogenous growth begins  $\sim 26$  days after the eruptive activity initiates (Hale and Wadge, 2008). In our simulations the time scale considered is shorter than the observational data. Our model simulation run time is constrained by the maximum stable mechanical time step ( $t = \sqrt{\frac{\text{mass of particle}}{k_n}}$ ) and the number of particles in the simulation. Considering the particle as a disk with thickness (equal to the characteristic width) in the simulation increases the time step, while the stress calculations are not altered by the mass increment of the particle (Itasca Consulting Group, 2004). The maximum time step in our model run is  $\sim 0.5 \text{ s}$  and the computational time increases with inclusion of additional particles. Thus, we consider a shorter time scale for the eruptive cycle to optimize the simulation time. Our modeled lava dome is simulated in 2-D geometry and is able to exhibit the various observed lava dome structures. The time scaling for the 2D model is accelerated over 3D that leads to a faster growth of the synthetic lava dome in the simulations. For a one to one correlation with observational data a 3-D DEM model is required. The development of a 3-D model is restricted by the significantly higher simulation time required to perform computational calculations. Our model provides a first order insight to the observed surface textures and explains some of the mechanistic behavior required to produce the various observed lava dome morphologies.

## 5.2. Controls on dome morphology

With a first-order understanding of the influence on material behavior exerted by extrusion rate, a simulation flow cycle is assumed (Fig. 15). The flow cycle follows a typical sequence of flow rates observed at Soufriere Hills Volcano. The assumed flow cycle initiates with a low extrusion rate ( $Q \sim 0.5 \text{ m}^3/\text{s}$ ) which then increases to  $\sim 4.0 \text{ m}^3/\text{s}$  before falling abruptly to a renewed declining background rate of 1.5 to  $0.5 \text{ m}^3/\text{s}$  before once again spiking to  $\sim 4.5 \text{ m}^3/\text{s}$ . This is followed by a rapid decline over  $\sim 4 \text{ h}$  to  $\sim 1 \text{ m}^3/\text{s}$ . The full cycle occurs over 55 h with the full flow history shown in Fig. 15. This sequence of flow rates produces distinctive growth patterns that reflect the variations in extrusion rate and corresponding changes in the mechanical properties of the material. Dome morphologies resulting from these simulations are in turn compared with those observed for dome growth at SHV (Fig. 17; Watts et al., 2002). The effusion history of Fig. 15 (labeled points A–H) is linked to snapshots of dome morphology in Fig. 16 (Table 5b). The various simulated dome morphologies reflect evolving magma rheologies, and thus comparisons can be made directly with field observations linked to observed extrusion rates (Fig. 17).

To accommodate the effects of degassing-induced stiffening due to variation in the flow rate history of magma, the material stiffness and strength were varied during the eruption cycle. Point a in Fig. 16 shows lava dome growth after 4.5 h of eruptive activity with flow rates of 0.5 to  $0.2 \text{ m}^3/\text{s}$ . Low extrusion rates ( $Q \leq 0.5 \text{ m}^3/\text{s}$ ) encourage magma degassing that leads to material stiffening and strength enhancement due to degassing induced crystallization (higher values of parallel bond stiffness and strength). The parallel bond stiffness of the material at low flow rates ( $Q \leq 0.5 \text{ m}^3/\text{s}$ ) is fixed at a high value (parallel bond stiffness =  $10^8 \text{ N/m}^3$ ), as the bulk modulus considered for

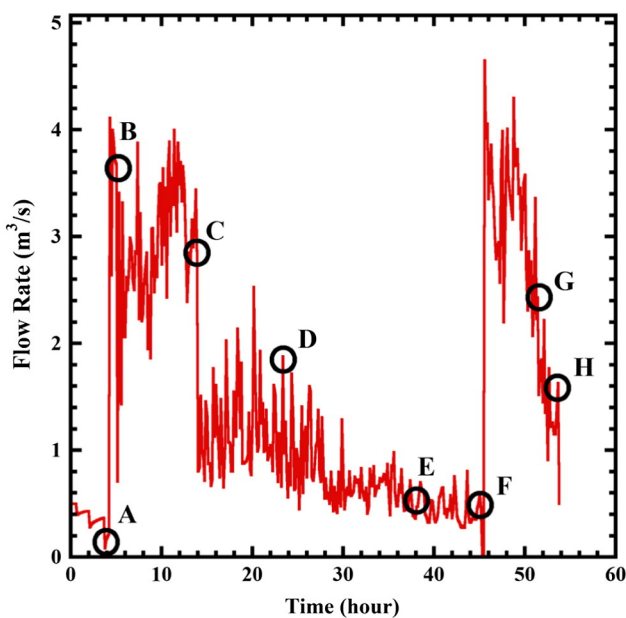


Fig. 15. Flow-rate history of the lava dome eruption cycle for the simulated run to represent lava dome growth with change in flow rate as represented by Watts et al. (2002). Snapshots of the modeled morphology are taken at points labeled from A to H.

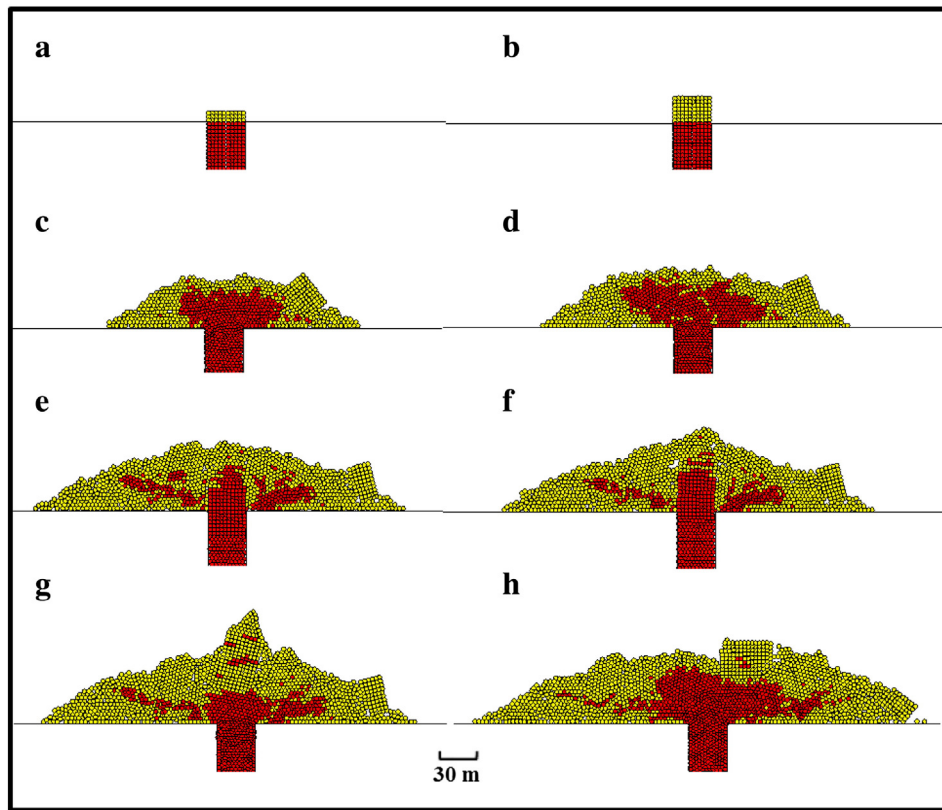


Fig. 16. Variation of magma rheology with change in flow rate as represented by the flow history of the eruption cycle given by Fig. 14.

extruded degassed material is high. The stiffer degassed lava extrudes as a spine at the conduit exit at the low flow rate (Table 5b).

A sudden influx of fresh magma into the conduit increases the average flow rate. The increase in high volatile content of the fresh magma pulse (low material stiffness at higher flow rate) results in the breakage of the parallel bonds of the old modeled lava particles in the dome. The breakage of the parallel bond reduces the effective bulk modulus for the material (Eq. (9)). Damage to the parallel bonds due to an increase in magma flow rate accumulates deformation at the base of the spine which in turn leads to collapse. At point b ( $t = 4.9$  h) the deformation at the base of the spine increases significantly resulting in collapse.

A fresh pulse of volatile rich magma degasses and solidifies and is assumed to form blocky lava (yellow particles) at the outer surface in the simulation. The rate of talus formation is controlled by the solidus pressure of the material (Eq. (10) and Fig. 4), which for andesitic lava is between 0.2 and 1 MPa (assumed here as 0.4 MPa) (Hale, 2008). Point b indicates the influx of a pulse of low-viscosity magma (low parallel bond stiffness and strength) which culminates in the collapse of the spine. This period (b to c) in the simulation represents the shear lobe type 1 growth pattern observed for volatile rich low viscosity magma for flow rates between 2 and 5  $\text{m}^3/\text{s}$  given in Fig. 17 (Watts et al., 2002). The field type is marked by broad spines observed at SHV developed over weeks to months, with intermittent exogenous and endogenous phases. While our simulation evolves over only a few hours (volume of the simulated lava dome is much smaller than the erupted volume at SHV), the observed morphology is consistent with field observations at SHV.

Point d represents flow at a diminished rate averaging about 1.3  $\text{m}^3/\text{s}$ . The resulting magma viscosity (interpreted via parallel bond stiffness and strength) at point d (lower flow rate) is higher than the viscosity of the magma infused at point c (higher flow rate) into the dome core during endogenous growth, but much lower viscosity than a degassed plug. A structure similar to a whale-back is inferred by shallow red particles (on left of the conduit).

At points e–f ( $t \sim 38$  to 45 h) a degassed lava plug begins to punch through the softer core material at a lower flow rate ( $Q \approx 0.5 \text{ m}^3/\text{s}$ ). At low flow rates, the magma extruded at the conduit exit is highly crystallized with a low volatile content and greater stiffness. The crystallized lava plug with high stiffness (with greater parallel bond strength) is able to punch its way through the softer core advancing in the direction of the created talus. Higher parallel bond stiffness is analogous to a material with greater viscosity, consistent with a degassed lava plug. Height of the resulting spine depends mainly on the flow duration, conditioned by material strength and increased stresses near the base of the spine (Voight, 2000). On re-ignition of the extrusion rate, the small section of the degassed lava plug is lifted by the pulse of fresh magma. The stiff lava plug punches through the overlying material and then collapses. The height and shape of the spine is a function of the magma flux and flow duration, and distribution of material strength and stiffness of the spine (cf. Voight, 2000 Figure 12). Consequently the height of the spine at point g and its collapse by point h is affected by the evolving strength and stiffness. The lava dome grows endogenously in h for a short time span as the flow drops as a consequence of assumed diminishing magma chamber overpressures.

The foregoing follows different growth patterns from spine generation to endogenous growth as a result of greater material stiffness at lower flow rates and reduced material stiffness at higher flow rates respectively. A first order understanding of the interplay of fundamental parameters (extrusion rate with material strength and stiffness) provides insight into the origin of various dome growth patterns and their dependency on antecedent effusive history.

## 6. Conclusions

Extrusion rate and magma rheology are known to exert significant control on patterns of cyclic growth and collapse of lava domes. Magma rheology is a strong function of temperature, pressure, composition, volatile content and crystal content. Thus magma ascent rates

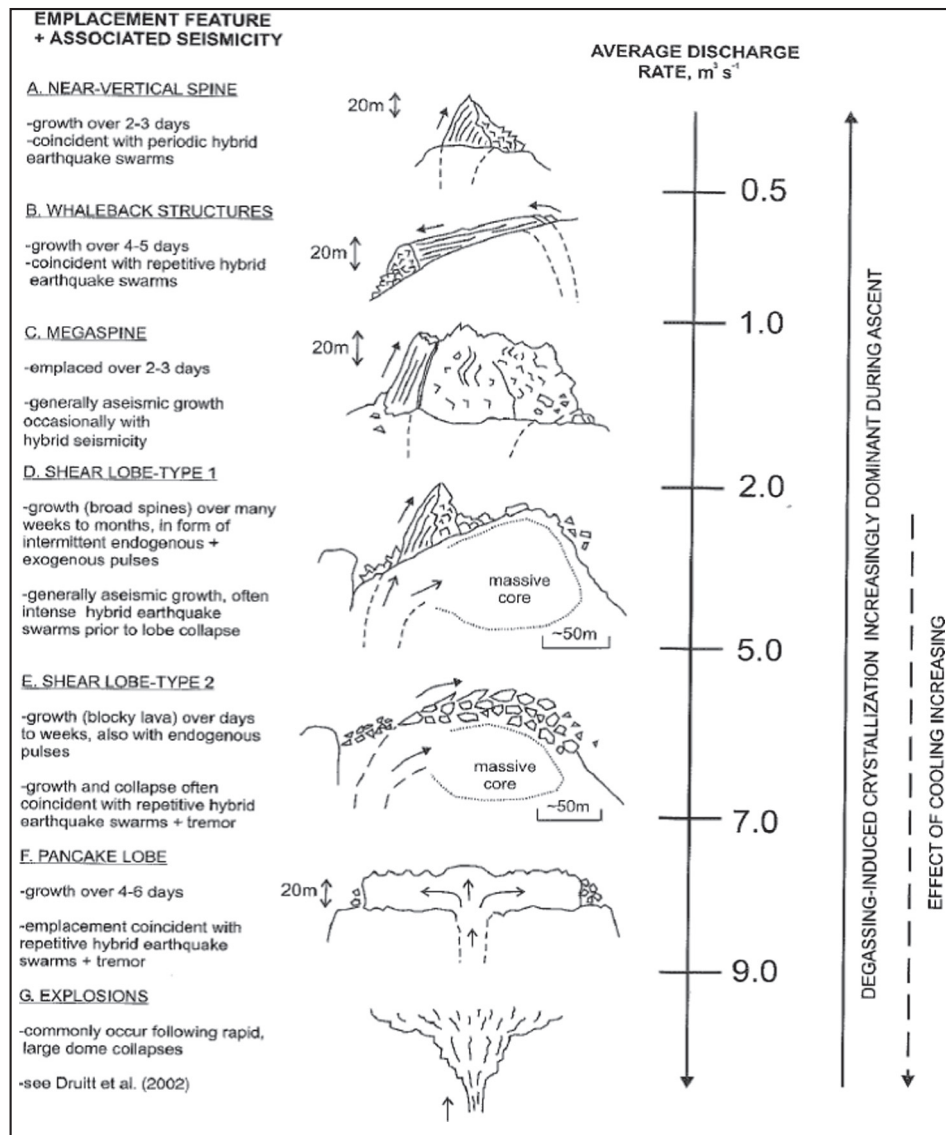


Fig. 17. Variation in the type of structure emplaced in relation to the average discharge rate, and the role of degassing-induced crystallization and cooling (Watts et al., 2002).

and decompression paths control magma texture which in turn governs magma rheology and contributes to the evolving morphology of the resulting lava dome. We present a model that incorporates the principal features of this evolution of strength and rheology into the spatial and temporal growth of a volcanic pile. This model provides a first order understanding of the effect of individual parameters on the mechanical strength and stiffness of the magma during the eruptive cycle. Material strength and stiffness of the magma comprising the soft dome core influences dome morphology more significantly than the frictional strength of the evolving talus comprising the carapace. The morphology

of the lava dome is sensitive to mechanical strength and stiffness – a small change in these parameters exerts a large influence on the pattern of growth. Transition from endogenous growth at high flow rates ( $Q \approx 3$  to  $7 \text{ m}^3/\text{s}$ ) to exogenous growth at lower flow rates ( $Q \approx 1$  to  $0.5 \text{ m}^3/\text{s}$ ) is shown to occur when ductile viscous material transforms to a stiffer rock due to degassing-induced crystallization that increases material stiffness and enhances strength. Material stiffness of the softer core is poorly constrained and the match between model and observations for the evolution of whale-back structures at SHV is currently more qualitative than quantitative.

Material stiffness and material strength are key control parameters which govern magma rheology and subsequently lava dome morphology. Our simulations mimic to a reasonable approximation the mechanistic behavior of different growth patterns observed at Soufriere Hills Volcano, Montserrat during the period June to July 1996, and thus provide insight and improved understanding of the interplay between material stiffness and material strength which is influenced by extrusion rate. Degassing-induced crystallization as observed at Soufriere Hills Volcano, Montserrat causes material stiffening and enhances material strength. The evolution of strength and stiffness in the material causes the ductile viscous material (core) to transform to a stiffer rock and is represented by increasing the parallel bond stiffness and strength. The

Table 5b

Parameter value considered for model run for the eruption cycle given by Fig. 15.

Period of eruption	Parallel bond stiffness ( $\text{N/m}^3$ )	Cohesion (MPa)	Pseudo/effective viscosity ( $\text{Pa}\cdot\text{s}$ )
Initiation–point A	$1 \times 10^8$	0.1	$3 \times 10^8$
Point B–point C	$4 \times 10^5$	0.4	$1.2 \times 10^6$
Point C–point D	$8 \times 10^5$	0.8	$2.4 \times 10^6$
Point D–point E	$2.5 \times 10^7$	10	$7.5 \times 10^7$
Point E–point F	$1 \times 10^8$	10	$3 \times 10^8$
Point F–point G	$1 \times 10^6$	0.4	$3 \times 10^6$
Point G–point H	$1 \times 10^6$	0.4	$3 \times 10^6$

increase in material stiffness and strength results in the transition of the rheology, from a soft ductile core growing endogenously to a stiffer and stronger material capable of punching through the overlying material at the conduit exit and generating a spine. The observed growth of spines occurs at low extrusion rate ( $Q \approx 0.5 \text{ m}^3/\text{s}$ ) for a material with high stiffness and greater material strength (Fig. 10). Simulation results in Section 5.1 (Fig. 13VI–X) represent the collapse of a stiff magma plug onto the talus on the influx of a pulse of volatile rich low viscosity magma. The resistance created by the overlying magma plug leads to the necessary formation of a new shear fault by the re-direction of magma flow along a new pathway. The structure of the simulated dome resembles the form interpreted for 27th July, 1996 at Soufriere Hills Volcano, Montserrat and shown by Fig. 12c (Watts et al., 2002).

The simulation results discussed in Section 5.2 indicate a strong correlation between extrusion rate and the subsequent effect on mechanical properties (material stiffness and strength) that lead to the variation in rheology which represents lava dome morphologies as observed at Soufriere Hills Volcano (Watts et al., 2002). Low viscosity magma flowing at relatively high flow rates ( $Q \approx 3$  to  $7 \text{ m}^3/\text{s}$ ) is incapable of punching through the overlying stiffer lava of the dome, thus resulting in endogenous dome growth evolving into the exogenous formation of blocky lava and represented by the simulation period from points B to C (Fig. 16) in Section 5.2. Low viscosity magma flowing at high flow rates is less stiff and is assigned lower bond stiffness and bond strength that causes breakage of parallel bond. This reduces the effective bulk modulus and results in relatively greater deformation of the ductile core material. Improved estimates of the mechanical properties of the core material will enhance the fidelity of the simulations. Our model may be improved to simulate endogenous growth and interior textures by including rheological models capable of tracking the development of mechanical properties with change in temperature, pressure and magma composition.

## Appendix A

### A.1. Correlation of normal stiffness ( $k_n$ ) with Young's modulus

Force–displacement equation is given by Eq. (11) as

$$f_n = -k_n \delta_n. \quad (11)$$

Young's modulus and deformation are related by Eq. (12)

$$f_n = -\frac{EA_o \Delta L}{L_o}. \quad (12)$$

Area perpendicular to the applied force is given by Eq. (13) (Fig. 1d)

$$A_o = D \cdot (w_C). \quad (13)$$

Thus, stiffness is given by Eq. (14)

$$k_n = \frac{ED(w_C)}{L_o}. \quad (14)$$

From Fig. 1d original length of sample is obtained and is given by Eq. (15)

$$L_o = D. \quad (15)$$

Therefore, stiffness is given Eq. (16)

$$k_n = E(w_C). \quad (16)$$

### A.2. Correlation of shear stiffness ( $k_s$ ) with shear modulus

The force–displacement equation is given by Eq. (17)

$$f_s = -k_s \delta_s. \quad (17)$$

The expression for shear modulus is given by Eq. (18)

$$f_s = -\frac{GA \Delta x}{L_o}. \quad (18)$$

Hence the correlation between shear stiffness and shear modulus is given by Eq. (19)

$$k_s = G(w_C). \quad (19)$$

### A.3. Correlation of 2D flow rate with actual 3D values

Average velocity of a fluid flowing through a pipe can be expressed by Hagen–Poiseuille's flow and is given by Eq. (20)

$$v_{3D} = \frac{Q_{3D}}{a_{3D}}. \quad (20)$$

If the flow velocity in the 2D model (specified in the simulation run) is maintained equal to the 3D value (Eq. (20)), then to correlate the flow rate in the 2 cases, an equivalent characteristic length/width is calculated. Characteristic length as shown in Fig. 1c is the width of the 2D model (which for most models is considered as unit thickness). The correlation is given by Eqs. (21) and (22)

$$\pi r^2 = L(w_C) \quad (21)$$

$$w_C = \frac{\pi r^2}{L}. \quad (22)$$

### A.4. Correlation of parallel bond stiffness with viscosity

The ductile core material is treated as a non-Newtonian fluid (Bingham fluid). The material flow initiates on the application of stress greater than the material yield stress ( $\tau_{max}$ ). The correlation of constant plastic viscosity with applied stress ( $\tau$ ) is given by

$$\Delta \tau = \tau - \tau_{max} = -\eta \frac{dV}{dy}. \quad (23)$$

If the change in shear stress ( $\Delta \tau$ ) is positive, then flow initiates and is affected by the parallel bond shear stiffness. Change in shear force for a given time step ( $\Delta t$ ) on the particle due to parallel bond shear stiffness is given by Eq. (24)

$$\Delta f^s = -k^s A \Delta U^s. \quad (24)$$

Change in shear displacement for a given time step in PFC<sup>2D</sup> is given by Eq. (25)

$$\Delta U^s = V_i \Delta t. \quad (25)$$

Change in shear stress due to parallel bond shear stiffness is given by Eq. (26)

$$\Delta \tau = -k^s V_i \Delta t. \quad (26)$$

Equating Eqs. (23) and (26)

$$-k^s V_i \Delta t = -\frac{\eta dV}{dy}. \quad (27)$$

Dividing both sides by length of the same ( $y$ ) results in Eq. (28) –

$$-k^s \Delta t y \frac{V_i}{y} = -\frac{\eta dV}{dy}. \quad (28)$$

In Eq. (28), the term  $\frac{V_i}{y}$  and  $\frac{dV}{dy}$  is the shear velocity per unit length of the material/fluid. Thus viscosity is related to parallel bond shear stiffness by Eq. (29)

$$\eta = k^s \Delta t y. \quad (29)$$

Hence parallel bond stiffness acts as the plastic viscosity term in the modeling of the bonded material. The effective plastic viscosity in the model is influenced by the time step value which is a function of the mass of the particle and the linear contact stiffness. Thus a change in the size of the time step affects the plastic viscosity of the modeled particle assemblage.

#### A.5. Correlation of microscopic modulus for particle–particle contact with contact stiffness

Using Eq. (16), the microscopic modulus of a particle–particle contact bond (in the absence of a parallel bond) is given by Eq. (30)

$$E_c = k_n (w_c). \quad (30)$$

#### A.6. Correlation of microscopic modulus for parallel bond with parallel bond stiffness

Parallel bond stiffness is expressed in units of stiffness per unit area and is given by Eq. (31)

$$k^n = E_p / L_0. \quad (31)$$

The original length of the particle system is expressed in Eq. (15). The microscopic modulus for parallel bond is given by Eq. (32)

$$E_p = k^n D. \quad (32)$$

## References

Anderson, S.W., Fink, J.H., 1990. The development and distribution of surface textures at the Mount St. Helens dome. In: Fink, J. (Ed.), *Lava Flows and Domes I/AVCEI Proceedings in Volcanology*. Springer, Berlin Heidelberg, pp. 25–46.

Annen, C., Lenat, J.F., Provost, A., 2001. The long-term growth of volcanic edifices: numerical modeling of the role of dyke intrusion and lava flow emplacement. *J. Volcanol. Geotherm. Res.* 105 (4), 263–289.

Barclay, J., Rutherford, M.J., Carroll, M.R., Murphy, M.D., Devine, J.D., Gardner, J., Sparks, R.S.J., 1998. Experimental phase equilibria constraints on pre-eruptive storage conditions of the Soufriere Hills magma. *Geophys. Res. Lett.* 25 (18), 3437–3440.

Blake, S., 1990. Viscoplastic models of lava domes. In: Fink, J.H. (Ed.), *Lava Flows and Domes: Emplacement Mechanisms and Hazard Implications*. Springer-Verlag, pp. 88–126.

Blundy, J., Cashman, K., 2001. Ascent driven crystallization of dacite magmas at Mount St. Helens, 1980–1986. *Contrib. Mineral. Petrol.* 140 (6), 631–650.

Blundy, J., Cashman, K., Humphreys, M., 2006. Magma heating by decompression driven crystallization beneath andesite volcanoes. *Nature* 443 (7107), 76–80.

Buisson, C., Merle, O., 2002. Experiments on internal strain in lava dome cross sections. *Bull. Volcanol.* 64 (6), 363–371.

Buisson, C., Merle, O., 2004. Numerical simulation of strain within lava domes. *J. Struct. Geol.* 26 (5), 847–853.

Caricchi, L., Burlini, L., Ulmer, P., Gerya, T., Vassalli, M., Papale, P., 2007. Non-Newtonian rheology of crystal-bearing magmas and implications for magma ascent dynamics. *Earth Planet. Sci. Lett.* 264 (3–4), 402–419.

Carn, S.A., Watts, R.B., Thompson, G., Norton, G.E., 2004. Anatomy of a lava dome collapse: the 20 March 2000 event at Soufriere Hills Volcano, Montserrat. *J. Volcanol. Geotherm. Res.* 131 (3–4), 241–264.

Cashman, K., Blundy, J., 2000. Degassing and crystallization of ascending andesite and dacite. *Philos. Trans. R. Soc. Lond. Ser. A* 1487–1513.

Cashman, K.V., Thornber, C.R., Pallister, J.S., 2008. From dome to dust: shallow crystallization and fragmentation of conduit mechanics during the 2004–2006 dome extrusion of Mount St. Helens, Washington. In: Sherrod, D.R., Scott, W.E., Stauffer, P.H. (Eds.), *A Volcano Rekindled: The Renewed Eruption of Mount St. Helens, 2004–2006*. U. S. Geological Survey, pp. 387–413.

Costa, A., 2005. Viscosity of high crystal content melts: dependence on solid fraction. *Geophys. Res. Lett.* 32, X1–X4.

Couch, S., Harford, C.L., Sparks, R.S.J., Carroll, M.R., 2003. Experimental constraints on the conditions of formation of highly calcic plagioclase microlites at the Soufriere Hills Volcano, Montserrat. *J. Petrol.* 44 (8), 1455–1475.

Cundall, P.A., Strack, O.D., 1979. A discrete numerical model for granular assemblies. *Geotechnique* 29 (1), 47–65.

de Michieli Vitturi, M., Clarke, A.B., Neri, A., Voight, B., 2010. Transient effects of magma ascent dynamics along a geometrically variable dome-feeding conduit. *Earth Planet. Sci. Lett.* 295 (3–4), 541–553.

Delenne, J.Y., Youssoufi, M.S.E., Cherblanc, F., Benet, J.C., 2004. Mechanical behavior and failure of cohesive granular materials. *Int. J. Numer. Anal. Methods Geomech.* 28 (15), 1577–1594.

Diller, K., Clarke, A.B., Voight, B., Neri, A., 2006. Mechanisms of conduit plug formation: implications for vulcanian explosions. *Geophys. Res. Lett.* 33 (20), L20302.

Dingwell, D.B., Romano, C., Hess, K.U., 1996. The effect of water on viscosity of a haplogranitic melt under P–T–X conditions relevant to silicic volcanism. *Mineral. Petrol.* 124 (1), 19–28.

Elsworth, D., Voight, B., 1992. Theory of dike intrusion in a saturated porous saturated porous solid. *J. Geophys. Res.* 97 (B6), 9105–9117.

Elsworth, D., Voight, B., 1995. Dike intrusion as a trigger for large earthquakes and the failure of volcano flanks. *J. Geophys. Res.* 100 (B4), 6005–6024.

Elsworth, D., Voight, B., 2001. The mechanics of harmonic gas pressurization and failure of lava domes. *Geophys. J. Int. Astron. Soc.* 145 (1), 187–198.

Elsworth, D., Voight, B., Thompson, G., Young, S.R., 2004. Thermal hydrologic mechanism for rainfall triggered collapse of lava domes. *Geology* 32 (11), 969–972.

Estep, J., Dufek, J., 2013. Discrete element simulations of bed force anomalies due to force chains in dense granular flows. *J. Volcanol. Geotherm. Res.* 254, 108–117.

Fink, J.H., Griffiths, R.W., 1990. Radial spreading of viscous gravity currents with solidifying crust. *J. Fluid Mech.* 221, 485–509.

Fink, J.H., Malin, M.C., Anderson, S.W., 1990. Intrusive and extrusive growth of the Mount St. Helens lava dome. *Nature* 348 (6300), 435–437.

Griffiths, R.W., 2000. The dynamics of lava flows. *Annu. Rev. Fluid Mech.* 32 (1), 477–518.

Griffiths, R.W., Fink, J.H., 1993. Effects of surface cooling on the spreading of lava flows and domes. *J. Fluid Mech.* 252, 667–702.

Griffiths, R.W., Fink, J.H., 1997. Solidifying Bingham extrusion: a model for the growth of silicic lava domes. *J. Fluid Mech.* 347, 13–36.

Guo, Y., Morgan, J.K., 2006. The frictional and micromechanical effects of grain comminution in fault gouge from distinct element simulations. *J. Geophys. Res.* 111 (B12), B12406 (12401–12421).

Hale, A.J., 2007. Magma flow instabilities in a volcanic conduit: implications for long-period seismicity. *Phys. Earth Planet. Inter.* 163 (1–4), 163–178.

Hale, A.J., 2008. Lava dome growth and evolution with an independently deformable talus. *Geophys. J. Int.* 174 (1), 391–417.

Hale, A.J., Mühlhaus, H.-B., 2007. Modelling shear bands in a volcanic conduit: implications for over-pressures and extrusion-rates. *Earth Planet. Sci. Lett.* 263 (1–2), 74–87.

Hale, A.J., Wadge, G., 2003. Numerical modelling of the growth dynamics of a simple silicic lava dome. *Geophys. Res. Lett.* 30 (19), SDE 11 (11–14).

Hale, A.J., Wadge, G., 2008. The transition from endogenous to exogenous growth of lava domes with the development of shear bands. *J. Volcanol. Geotherm. Res.* 171 (3–4), 237–257.

Hale, A.J., Bourgoin, L., Mühlhaus, H.B., 2007. Using the level set method to model endogenous lava dome growth. *J. Geophys. Res. Solid Earth* 112 (B3), B03213 (03211–03216).

Hammer, J.E., Rutherford, M.J., 2002. An experimental study of the kinetics of decompression-induced crystallization in silicic melt. *J. Geophys. Res.* 107 (B1) (ECV 8–1–ECV 8–24).

Hammer, J.E., Cashman, K.V., Voight, B., 2000. Magmatic processes revealed by textural and compositional trends in Merapi dome lavas. *J. Volcanol. Geotherm. Res.* 100 (1–4), 165–192.

Hess, K.-U., Dingwell, D.B., 1996. Viscosities of hydrous leucogranitic melts: a non-Arrhenian model. *Am. Mineral.* 81, 1297–1300.

Hort, M., 1998. Abrupt change in magma liquidus temperature because of volatile loss or magma mixing: effects on nucleation, crystal growth and thermal history of the magma. *J. Petrol.* 39 (5), 1063–1076.

Huppert, H.E., Woods, A.W., 2002. The role of volatiles in magma chamber dynamics. *Nature* 420, 493–495.

Huppert, H.E., Shepherd, J.B., Haraldur Sigurdsson, R., Sparks, S.J., 1982. On lava dome growth, with application to the 1979 lava extrusion of the Soufriere of St. Vincent. *J. Volcanol. Geotherm. Res.* 14 (3–4), 199–222.

Innocenti, S., Andreastuti, S., Furman, T., del Marmol, M.A., Voight, B., 2013a. The pre-eruption conditions for explosive eruptions at Merapi volcano as revealed by crystal texture and mineralogy. *J. Volcanol. Geotherm. Res.* 261, 69–86.

Innocenti, S., del Marmol, M.A., Voight, B., Andreastuti, S., Furman, T., 2013b. Textural and mineral chemistry constraints on evolution of Merapi Volcano, Indonesia. *J. Volcanol. Geotherm. Res.* 261, 20–37.

Itasca Consulting Group, Inc., 2004. *User's Guide, PFC2d* Itasca Consulting Group, Inc.

Iverson, R.M., 1990. Lava domes modeled as brittle shells that enclose pressurized magma, with application to Mount St. Helens. In: Fink, J.H. (Ed.), *Lava Flows*

- and Domes: Emplacement Mechanisms and Hazard Implications. Springer-Verlag, pp. 47–69.
- Jaupart, C., 1998. Gas loss through magmas through conduit walls during eruption. In: Gilbert, J.S., Sparks, R.S.J. (Eds.), *The Physics of Explosive Volcanic Eruptions*. The Geological Society, pp. 73–90.
- Lavallee, Y., Hess, K., Cordonnier, B., Dingwell, D., 2007. Non-Newtonian rheological law for highly crystalline dome lavas. *Geology* 35 (9), 843–846.
- Lejeune, A.-M., Richet, P., 1995. Rheology of crystal-bearing silicate melts: an experimental study at high viscosities. *J. Geophys. Res. Solid Earth* 100 (B3), 4215–4229.
- Loughlin, S.C., Lockett, R., Ryan, G., Christopher, T., Hards, V., De Angelis, S., Jones, L., Strutt, M., 2010. An overview of lava dome evolution, dome collapse and cyclicity at Soufriere Hills Volcano, Montserrat, 2005–2007. *Geophys. Res. Lett.* 37 (19), 1–6.
- Martel, C., Schmidt, B.C., 2003. Decompression experiments as an insight into ascent rates of silicic magmas. *Contrib. Mineral. Petrol.* 144 (4), 397–415.
- Melnik, O., Sparks, R.S.J., 1999. Nonlinear dynamics of lava dome extrusion. *Nature* 402, 37–41.
- Melnik, O., Sparks, R.S.J., 2002. Dynamics of magma ascent and lava extrusion at Soufriere Hills Volcano, Montserrat. In: Druitt, H.T., Kokelaar, B.P. (Eds.), *The Eruption of Soufriere Hills Volcano, Montserrat From 1995 to 1999*. The Geological Society, London, pp. 153–171.
- Melnik, O., Sparks, R.S.J., 2005. Controls on conduit magma flow dynamics during lava dome building eruptions. *J. Geophys. Res.* 110 (B2), B02209–B02231.
- Melnik, O., Barmin, A.A., Sparks, R.S.J., 2005. Dynamics of magma flow inside volcanic conduits with bubble overpressure buildup and gas loss through permeable magma. *J. Volcanol. Geotherm. Res.* 143, 53–68.
- Morgan, J.K., McGovern, P.J., 2005a. Discrete element simulations of gravitational volcanic deformation : 1. Deformation structures and geometries. *J. Geophys. Res.* 110 (B5), 1–22.
- Morgan, J.K., McGovern, P.J., 2005b. Discrete element simulations of gravitational volcanic deformation : 2. Mechanical analysis. *J. Geophys. Res.* 110 (B5), 1–13.
- Petford, N., 2003. Rheology of the granitic magmas during ascent emplacement. *Annu. Rev. Earth Planet. Sci.* 31, 399–427.
- Rutherford, M.J., Devine, J.D., 2003. Magmatic conditions and Magmatic ascent as indicated by hornblende phase equilibria and reactions in the 1995–2002 Soufriere Hills magma. *J. Petrol.* 44 (8), 1433–1454.
- Ryan, G.A., Loughlin, S.C., James, M.R., Jones, L.D., Calder, E.S., Christopher, T., Strutt, M.H., Wadge, G., 2010. Growth of the lava dome and extrusion rates at Soufriere Hills Volcano, Montserrat, West Indies: 2005–2008. *Geophys. Res. Lett.* 37 (19), 1–5.
- Saar, M.O., Manga, M., Cashman, K.V., Fremouw, S., 2001. Numerical models of the onset of yield strength in crystal–melt suspensions. *Earth Planet. Sci. Lett.* 187 (3–4), 367–379.
- Samuelson, J., Marone, C., Voight, B., Elsworth, D., 2008. Laboratory investigation of the frictional behavior of granular volcanic material. *J. Volcanol. Geotherm. Res.* 173 (3–4), 265–279.
- Shen, A.Q., 1998. *Mathematical and Analog Modeling of Lava Dome Growth*. University of Illinois, Urbana-Champaign.
- Simmons, J., Elsworth, D., Voight, B., 2004. Instability of exogenous lava lobes during intense rainfall. *Bull. Volcanol.* 66 (8), 725–734.
- Simmons, J., Elsworth, D., Voight, B., 2005. Classification and idealized limit-equilibrium analyses of dome at Soufriere Hills volcano, Montserrat, during growth of the first lava dome: November 1995–March 1998. *J. Volcanol. Geotherm. Res.* 139 (3–4), 241–258.
- Sparks, R.S.J., 1997. Causes and consequences of pressurization in lava dome eruptions. *Earth Planet. Sci. Lett.* 150 (3–4), 177–189.
- Sparks, R.S.J., Young, S.R., Barclay, J., Calder, E.S., Cole, P., Darroux, B., Davies, M.A., Druitt, T.H., Harford, C., Herd, R., James, M., Lejeune, A.M., Loughlin, S., Norton, G., Skerrett, G., Stasiuk, M.V., Toothill, J., Wadge, G., Watts, R., 1998. Magma production and growth of the lava dome of the Soufriere Hills Volcano, Montserrat, West Indies: November 1995 to December 1997. *Geophys. Res. Lett.* 25 (18), 3421–3424.
- Sparks, R.S.J., Murphy, M.D., Lejeune, A.M., Watts, R.B., Barclay, J., Youngs, S.R., 2000. Control on the emplacement of the andesite lava dome of the Soufriere Hills volcano, Montserrat by degassing induced crystallization. *Terra Nova* 12 (1), 14–20.
- Sporli, K.B., Rowland, J.V., 2006. Column on column structures as indicators of lava/ice interaction, Ruapehu andesite volcano, New Zealand. *J. Volcanol. Geotherm. Res.* 157 (4), 294–310.
- Swanson, D.A., Holcomb, R.T., 1990. Regularities in growth of the Mount St. Helens Dacite Dome. In: Fink, J. (Ed.), *Lava Flows and Domes*. IAVCEI Proceedings in Volcanology. Springer, Berlin Heidelberg, pp. 25–46.
- Tuffen, H., Dingwell, D., 2005. Fault textures in volcanic conduits: evidence for seismic trigger mechanisms during silicic eruptions. *Bull. Volcanol.* 67 (4), 370–387.
- Voight, B., 2000. Structural stability of andesite volcanoes and lava domes. *Philos. Trans. R. Soc. Lond.* 358, 1663–1703.
- Voight, B., Elsworth, D., 1997. Failure of volcano slopes. *Geotechnique* 47 (1), 1–31.
- Voight, B., Elsworth, D., 2000. Instability and collapse of hazardous gas pressurized lava domes. *Geophys. Res. Lett.* 27 (1), 1–4.
- Voight, B., Sparks, R.S.J., Miller, A.D., Stewart, R.C., Hoblitt, R.P., Clarke, A., Ewart, J., Aspinall, W.P., Baptie, B., Calder, E.S., Cole, P., Druitt, T.H., Hartford, C., Herd, R.A., Jackson, P., Lejeune, A.M., Lockhart, A.B., Loughlin, S.C., Lockett, R., Lynch, L., Norton, G.E., Robertson, R., Watson, I.M., Watts, R., Young, S.R., 1999. Magma flow instability and cyclic activity at Soufriere Hills Volcano, Montserrat, British West Indies. *Science* 283 (5405), 1138–1142.
- Voight, B., Komorowski, J.-C., Norton, G.E., Belousov, A.B., Belousova, M., Boudon, G., Francis, P.W., Franz, W., Heinrich, P., Sparks, R.S.J., Young, S.R., 2002. The 26th December (Boxing Day) 1997 sector collapse and debris avalanche at Soufriere Hills Volcano, Montserrat. In: Druitt, T.H., Kokelaar, B.P. (Eds.), *The Eruption of Soufriere Hills Volcano, Montserrat, From 1995 to 1999*. The Geological Society, London, pp. 363–407.
- Wadge, G., Herd, R., Calder, E.S., Komorowski, J.-C., 2010. Lava production at Soufriere Hills Volcano, Montserrat: 1995–2009. *Geophys. Res. Lett.* 37 (19), 1–5.
- Watts, R.B., Herd, R.A., Sparks, R.S.J., Young, S.R., 2002. Growth patterns and emplacement of the andesitic lava dome at Soufriere Hills Volcano, Montserrat. In: Druitt, T.H., Kokelaar, B.P. (Eds.), *The Eruption of Soufriere Hills Volcano, Montserrat, From 1995–1999*. Geological Society Memoir No. 21, pp. 115–152.
- Widiwijayanti, C., Clarke, A., Elsworth, D., Voight, B., 2005. Geodetic constraints on the shallow magma system at Soufriere Hills Volcano, Montserrat. *Geophys. Res. Lett.* 32 (11), L11309 (11301–11305).
- Woods, A.W., Huppert, H.E., 2003. On magma chamber evolution during slow effusive eruptions. *J. Geophys. Res.* 108 (B8) (ECV 12–11–ECV 12–16).